On the Three-dimensional Structure of Local Molecular Clouds

Catherine Zucker[1] , Alyssa Goodman[1] , João Alves[2] , Shmuel Bialy[1] , Eric W. Koch[1,3] , Joshua S. Speagle[1,4,5,6] ,
Michael M. Foley[1] , Douglas Finkbeiner[1] , Reimar Leike[7,8] , Torsten Enßlin[7,8] , Joshua E. G. Peek[9,10] , and
Gordian Edenhofer[7,8]

[1] Center for Astrophysics, Harvard & Smithsonian, 60 Garden Street, Cambridge, MA 02138, USA; catherine.zucker@cfa.harvard.edu
[2] University of Vienna, Department of Astrophysics, Türkenschanzstraße 17, A-1180 Vienna, Austria
[3] University of Alberta, Department of Physics, 4-183 CCIS, Edmonton, AB T6G 2E1, Canada
[4] Department of Statistical Sciences, University of Toronto, Toronto, ON M5S 3G3, Canada
[5] David A. Dunlap Department of Astronomy & Astrophysics, University of Toronto, Toronto, ON M5S 3H4, Canada
[6] Dunlap Institute for Astronomy & Astrophysics, University of Toronto, Toronto, ON M5S 3H4, Canada
[7] Max Planck Institute for Astrophysics, Karl-Schwarzschildstraße 1, D-85748 Garching, Germany
[8] Ludwig-Maximilians-Universität, Geschwister-Scholl Platz 1, D-80539 Munich, Germany
[9] Space Telescope Science Institute, 3700 San Martin Drive, Baltimore, MD 21218, USA
[10] Department of Physics & Astronomy, Johns Hopkins University, Baltimore, MD 21218, USA

Abstract

We leverage the 1 pc spatial resolution of the Leike et al. three-dimensional (3D) dust map to characterize the 3D structure of nearby molecular clouds ($d \lesssim 400$ pc). We start by "skeletonizing" the clouds in 3D volume density space to determine their "spines," which we project on the sky to constrain cloud distances with $\approx 1\%$ uncertainty. For each cloud, we determine an average radial volume density profile around its 3D spine and fit the profiles using Gaussian and Plummer functions. The radial volume density profiles are well described by a two-component Gaussian function, consistent with clouds having broad, lower-density outer envelopes and narrow, higher-density inner layers. The ratio of the outer to inner envelope widths is $\approx 3{:}1$. We hypothesize that these two components may be tracing a transition between atomic and diffuse molecular gas or between the unstable and cold neutral medium. Plummer-like models can also provide a good fit, with molecular clouds exhibiting shallow power-law wings with density, n, falling off like n^{-2} at large radii. Using Bayesian model selection, we find that parameterizing the clouds' profiles using a single Gaussian is disfavored. We compare our results with two-dimensional dust extinction maps, finding that the 3D dust recovers the total cloud mass from integrated approaches with fidelity, deviating only at higher levels of extinction ($A_V \gtrsim 2$–3 mag). The 3D cloud structure described here will enable comparisons with synthetic clouds generated in simulations, offering unprecedented insight into the origins and fates of molecular clouds in the interstellar medium.

Unified Astronomy Thesaurus concepts: Molecular clouds (1072); Solar neighborhood (1509); Interstellar reddening (853); Astronomy data visualization (1968)

Supporting material: interactive figures

1. Introduction

Much of our understanding of the structure and properties of molecular clouds is obtained via either two-dimensional (2D) observations of dust in emission or extinction (see Lombardi 2009; André et al. 2010; Planck Collaboration et al. 2011) or three-dimensional (3D) spectral-line observations of gas (see Dame et al. 2001), where the third dimension is not distance, but radial velocity. Until very recently, any insights into the true 3D spatial structure of molecular clouds were available only in numerical simulations, and were limited by the extent to which these simulations could approximate the observed properties of real clouds. Even then, detailed comparisons between observations and simulations could, again, only be made either in 2D projected space, or via spectral line maps, where the correspondence of intensity features in position–position–velocity (PPV) space to "real" density features in position–position–position (PPP) space has been shown to be fraught with complications (Beaumont et al. 2013).

Interstellar dust reddens starlight, so by *simultaneously* modeling the distance and extinction to large numbers of stars, it is possible to infer a self-consistent 3D distribution of stars and dust that produces the observed distribution of stellar colors. Prior to the advent of

Gaia (Gaia Collaboration et al. 2018) in 2018, accurate (e.g., astrometric) measurements of stars' distances independent from measures of their colors were scarce, so transforming the 2D sky into a 3D physical picture of the distribution of stars and clouds that form them was extraordinarily challenging statistically. Several path-breaking 3D dust maps were created prior to Gaia (Marshall et al. 2006; Sale et al. 2014; Green et al. 2015), but Gaia's astrometric constraints on stellar distances have allowed for significant gains in the spatial resolution of 3D dust maps. The fidelity of 3D maps has improved even more as a variety of photometric catalogs, which offer billions of stellar color measurements needed to constrain extinction in fits, have been cross-matched with Gaia, (see, e.g., Rezaei Kh. et al. 2018; Chen et al. 2019; Green et al. 2019; Lallement et al. 2019; Leike & Enßlin 2019; Hottier et al. 2020). Customization of the 3D dust-mapping framework, where distance resolution can be enhanced at the expense of spatial resolution, has yielded highly accurate distance measurements for nearby molecular clouds, with typical distance uncertainties of $\approx 5\%$ (Yan et al. 2019; Zucker et al. 2019, 2020; Chen et al. 2020), a factor of five improvement over typical distance uncertainties in the pre-Gaia era.

While these new catalogs of molecular cloud distances have shown good agreement with maser distances (Zucker et al. 2020),

revealed new Galactic-scale features (e.g., the Radcliffe Wave; Alves et al. 2020), and even mapped distance gradients *within* an individual molecular cloud (Zucker et al. 2018b, 2019), up until now catalogs have not had the resolution to resolve the detailed 3D structure (e.g., thickness, orientation) of clouds on scales comparable to numerical simulations. Most existing approaches group batches of stars into pixels *on the sky*, and then fit stellar distance and extinction measurements in each pixel to obtain the distribution of dust along the line of sight. A 3D map can then be created by combining 1D line-of-sight information for all 2D sky pixels. However, the line-of-sight dust distributions suffer from a distortion effect, where the angular resolution on the sky is always superior to the distance resolution along the line of sight, resulting in dust clouds appearing to extend radially outward from the Sun in an unphysical manner.

Recently Leike et al. (2020a) presented a new 3D dust map of the solar neighborhood out to a distance of $\approx$400 pc with a distance resolution of 1 pc. Leike et al. (2020a) overcame the "fingers of god" effect by directly modeling the dust density in 3D x–y–z cartesian space. Their method combines metric Gaussian variational inference (Knollmüller & Enßlin 2019) with Gaussian Processes (e.g., Rasmussen & Williams 2006) in the context of information field theory (see Enßlin et al. 2009; Enßlin & Frommert 2011; Arras et al. 2019; Enßlin 2019). The integrated extinction for a star known to lie in a given 3D voxel with some uncertainty provides information on the integrated dust density along that given line of sight, acting as an "anchor" point that can constrain the smooth 3D distribution of dust. By inferring the spatial correlation of the dust on different scales, one can connect these anchor points, and infer the dust distribution at arbitrary points in space, including along lines of sight where no stars are observed. Specifically, Leike et al. (2020a) modeled the dust as a log-normal Gaussian process, while *simultaneously* inferring the correlation kernel of the process, corresponding to the physical spatial correlation power spectrum of the dust. In this way, Leike et al. (2020a) used information on the distance and extinction to 5 million stars in the vicinity of the Sun (obtained from the Starhorse algorithm; see Anders et al. 2019) to reconstruct the 3D spatial distribution of dust on a fixed cartesian grid with a spatial resolution of 1 pc. The Leike et al. (2020a) results offer the first clear 3D spatial view of the local interstellar medium.[11]

In this work, we utilize the high spatial resolution of the Leike et al. (2020a) 3D dust map to analyze the 3D spatial structure and thicknesses of famous nearby star-forming regions for the first time. Specifically, we extend two existing algorithms geared toward 2D data—`FilFinder` (Koch & Rosolowsky 2015) and `RadFil` (Zucker & Chen 2018a)—into 3D. We apply the `FilFinder3D` algorithm to determine the topological skeletons of nearby clouds. We then use `Rad-Fil3D` to determine their average radial volume density profiles, and characterize the shapes of these profiles via both Gaussian and Plummer fitting. We then validate our results by creating synthetic 2D dust extinction maps from the 3D density distributions, and comparing these maps to independent results (derived from the Near-Infrared Color Excess Method Tailored

for Small-Scale Structures (NICEST) algorithm; Lombardi 2009; Lombardi et al. 2011) often used in star formation studies of nearby molecular clouds.

In Section 2, we present the data sets used in this work, including the Leike et al. (2020a) dust map and the NICEST 2D extinction maps. In Section 3, we detail the methodology we use to derive the topological spines of the clouds, and to construct radial volume density profiles for each region. We also discuss the derivation of our 2D extinction maps. In Section 4, we present our results in the context of a custom 3D visualization environment, including the x–y–z–l–b–d values (the Heliocentric Galactic Cartesian coordinates, the Galactic coordinates, and the distance) for each point in the spine of every cloud, and their thicknesses derived from the radial profile fitting. We also compare the 2D dust extinction maps derived from the projected Leike et al. (2020a) 3D dust distribution with NICEST 2D extinction maps, compute cloud masses from each method, and quantify the dynamic range in density that the Leike et al. (2020a) dust map is able to probe. In Section 6, we discuss the implications of our results, including potential evidence of a phase transition in our radial density profiles. Finally, we conclude in Section 7.

2. Data

2.1. Leike et al. (2020a) 3D Dust Map

Leike et al. (2020a) computed the 3D dust distribution on a cartesian grid centered on the Sun, extending $x = [-370$ pc, 370 pc], $y = [-370$ pc, 370 pc], and $z = [-270$ pc, 270 pc], where x, y, and z are the Heliocentric Galactic Cartesian coordinates. As such, the distance range of the map varies from $d = 370$ pc in the midplane, up to $d \approx 590$ pc at the corners of the grid. This distance range encompasses about a dozen well-studied nearby star-forming regions, and in this work we target the Chamaeleon, Ophiuchus, Orion B, Orion A, λ Orionis, Lupus, Taurus, Perseus, Musca, Pipe, and Cepheus molecular clouds for our radial profile analyses. We also provide the topological skeleton for one additional cloud—Corona Australis—but do not fit for its width, because it does not meet the density threshold required for inclusion in our study (see Section 3.1). We emphasize that three clouds—Orion A, Orion B, and λ Orionis—lie at the very edge of the Leike et al. (2020a) grid, and the results for these clouds are subject to additional scrutiny, as discussed further in Section 4.

2.1.1. Converting to Gas Volume Density

The Leike et al. (2020a) 3D dust map is provided in terms of the differential extinction, specifically the optical depth in the Gaia G-band, τ_G, per one parsec. Leike et al. (2020a) generated 12 samples of their 3D dust map, and we adopt the mean of the samples in our main analysis. To ensure that uncertainties in the underlying dust reconstruction are not affecting our results, we will additionally repeat our radial profile analysis using all 12 realizations of the dust map, as discussed further in Appendix E.[12]

There are several steps needed to convert the data values of the mean map—referred to as the extinction density s_x in Leike et al. (2020a)—to gas volume density. First, we use the relationship between $\frac{A_\lambda}{N_H}$ (the ratio of the extinction A at some

---

[11] The methodology is similar to that summarized in Rezaei Kh. et al. (2017, 2018) and implemented in Rezaei Kh. et al. (2020) to obtain a 3D cartesian view of the Orion A molecular cloud at a spatial resolution of approximately 10 pc. We will compare the Leike et al. (2020a) results to the Rezaei Kh. et al. (2020) results in Orion A in Section 5.

[12] For more details, see the public release of the Leike et al. (2020a) map available on Zenodo (Leike et al. 2020b). The mean dust map is available in the `mean_std.h5` file, while the 12 samples are available in `samples.h5`.

wavelength λ over the hydrogen column density N_H) and inverse wavelength from Draine (2009, see their Figure 1). Assuming a mean wavelength for the Gaia G-band of 673 nm ($\lambda^{-1} = 1.49\,\mu m^{-1}$; Jordi et al. 2010), we obtain $\frac{A_G}{N_H} = 4 \times 10^{-22}\,cm^2$ mag from Draine (2009).[13] Given the known relationship between extinction A_G and optical depth ($A_G = 1.086 \times \tau_G$) we obtain $N_H = 2.71 \times 10^{21}\,\tau_G\,cm^{-2}$. Finally, given that the Leike et al. (2020a) map is provided in the form of $\frac{\tau_G}{1\,pc}$ (rather than the usual τ_G), we obtain $n_H = 880\,cm^{-3} \times s_x$. Thus, to convert the Leike et al. (2020a) 3D dust map to volume density of hydrogen, we simply multiply the entire volume by a factor of 880. We emphasize that this volume density is the total volume density of hydrogen nuclei, independent of phase ($n = n_{H\,I} + 2n_{H_2}$) and is used to derive all results reported in Section 4. Volume density cubes for each cloud, with World Coordinate System (WCS) information in a cartesian reference frame, are available on the Harvard Dataverse (see https://doi.org/10.7910/DVN/IADP7W).

2.1.2. Systematic Effects

While Leike et al. (2020a) provided their results on a 1 pc grid, they argued that the functional resolution of the map is 2 pc, and only features which manifest at spatial scales greater than 2 pc should be considered reliable. Accordingly, for the main analysis, we exclude the inner 2 pc of each dust cloud's radial volume density profile when inferring their structure, while reporting results including the inner 2 pc in Appendix D.

By performing tests on synthetic mock data, Leike & Enßlin (2019) and Leike et al. (2020a) also found that there are a small number of outliers in their 3D dust distribution, in which the differential dust extinction values in certain voxels is significantly larger than predicted, to a degree that cannot be captured by the reported uncertainties. While Leike & Enßlin (2019) and Leike et al. (2020a) used different underlying stellar data for their statistical reconstruction, the methodology is similar, and we find the same high-differential-extinction outliers in the newer Leike et al. (2020a) map. In this analysis, we will be averaging over many voxels and will find that our results are insensitive to these outliers.

We emphasize that the *3D volume densities reported here are likely lower limits*. We observe inhomogeneities in column density maps of nearby molecular clouds at spatial scales smaller than 2 pc, the effective spatial resolution of the Leike et al. (2020a) 3D dust map (see, e.g., Zari et al. 2016). Thus, much of the dense gas in these clouds is unresolved, not just due to the map's spatial resolution, but due to the inability of the 3D dust-mapping technique to probe high-density gas, stemming from the lack of stellar data constraining the 3D dust reconstruction in this regime.

Finally, one additional consideration is the effect that young stellar objects (YSOs) have on the 3D dust reconstruction in Leike et al. (2020a) and whether this would bias any 3D volume density estimates. The stellar catalog underpinning Leike et al. (2020a) is based on the StarHorse algorithm, presented in Anders et al. (2019). Anders et al. (2019) did not employ any pre-main-sequence models when determining stellar properties. Thus, as argued in Anders et al. (2019), any young stars detected with Gaia and included in the StarHorse sample will have poor fits,

triggering a reliability flag. As Leike et al. (2020a) only used high-quality stellar data with no questionable reliability flags set, there should be very little contamination from YSOs in the 3D dust map.

2.2. 2D NICEST Extinction Maps

To validate our 3D cloud structure results (see Section 3) and quantify any "missing mass" in the 3D maps, we compute 2D maps of the K-band extinction, A_K, using the NICEST algorithm (Lombardi 2009) for each cloud. Goodman et al. (2009) showed that dust extinction estimates based on the near-infrared color excess are relatively free from bias and provide more robust estimates of the column density, at higher dynamic range, than gas-based approaches. NICEST, and its predecessor the Near-Infrared Color Excess Revisited (NICER) algorithm (Lombardi & Alves 2001), rely on the fact that the difference between the observed and intrinsic colors of a star (background to a cloud) provide information on the cloud's extinction along the line of sight to that star. By measuring the unreddened colors of stars in a nearby, low-extinction control field, it is possible to model the color excess on a star-by-star basis. Because there is a small dispersion in the intrinsic near-infrared colors of stars (and photometric errors), the technique requires averaging the extinction estimates for many individual stars in batches across the cloud, and pixel-by-pixel extinction estimates are computed as spatial averages via the adoption of a Gaussian smoothing kernel. Compared to NICER, NICEST removes contamination by foreground stars, which by their nature do not probe the cloud's extinction, and better characterizes small-scale inhomogeneities (i.e., filaments) present in the dust.

Like Lombardi et al. (2011), to compute the extinction we leverage the near-infrared J-, H-, and K-band colors of millions of stars detected in the Two Micron All-Sky Survey (2MASS; Skrutskie et al. 2006) for each field. Using the 2MASS photometry, NICEST creates two sets of stellar samples: main-sequence stars and YSOs, defined using their respective K-band magnitude distributions. In practice, given a star, the algorithm computes the intrinsic K-band magnitude (i.e., removes the extinction) and compares this with the K-band number counts of field stars (typically an exponential distribution) and YSOs (typically a Gaussian-like curve). This comparison is used to assign to each star a probability of being a YSO. The functionality to produce custom cloud-by-cloud NICEST extinction maps is available online (Lombardi & Alves 2001; Lombardi 2009)[14] and we adopt the default map making and cluster parameters. The default option is to include all stars in the extinction calculation, including YSOs. To check that YSOs are not affecting our mass calculations, we compute two masses for Orion A both with and without including YSOs in the sample. We find that including the YSOs in the extinction calculation only increases the mass by 2%. Because Orion A contains the largest number of YSOs in the solar neighborhood, our decision to compute the extinction maps using all stars should have no effect on our results. The configuration files used to produce the NICEST maps are available online at the Harvard Dataverse; the NICEST maps for all clouds targeted in this study are likewise available online (see https://doi.org/10.7910/DVN/WONVUH for both).

---

[13] Draine (2009) assumed an $R_V = 3.1$. Thus, variation in R_V could induce changes in our adopted conversion to gas volume density.

[14] See http://interstellarclouds.fisica.unimi.it/html/index.html.

3. Methods

3.1. FilFinder 3D

To determine the topological skeletons of nearby molecular clouds, we employ a modified 3D version of the FilFinder package from Koch & Rosolowsky (2015). FilFinder was originally developed in 2D to constrain the filamentary structure in H_2 column density maps obtained as part of the Herschel Gould Belt Survey (André et al. 2010). FilFinder3D uses similar morphological operations to the existing 2D version, but now employs the skan package for efficient operations on large morphological skeletons (Nunez-Iglesias et al. 2018). A full description of the 3D algorithm will be presented in E. W. Koch et al. (2021, in preparation).

To compute the skeletons, we start by defining the same density threshold for all clouds, equivalent to $n = 35\,cm^{-3}$, based on the volume density distribution computed in Section 2.1.[15] Hierarchical structure-finding algorithms for feature identification do exist for 3D volumes, the most common being dendrograms (Rosolowsky et al. 2008), which are frequently applied to spectral-line cubes of CO emission in PPV space (Rice et al. 2016). However, it is well known that dendrograms are not able to capture filamentary structure, with rarely any structures exceeding an aspect ratio of 2:1 (see Rice et al. 2016). Because we find that nearby star-forming regions are indeed filamentary, even at lower densities, we forgo dendrograms for this analysis and defer to future work. Before settling on a fixed threshold of $n = 35\,cm^{-3}$, we test a variety of thresholds, ranging from 20 to $50\,cm^{-3}$. Thresholds that are significantly higher than $n = 35\,cm^{-3}$ were too patchy to skeletonize, while thresholds that are significantly lower than $n = 35\,cm^{-3}$ meant that the peak radial densities were often offset from the main spine.[16] Our choice of density threshold is validated in Section 4, as the spines defined in 3D tend to align very well with the spines of filaments seen in 2D dust emission from Planck (Planck Collaboration et al. 2011), and the radial density profiles peak near a radial distance of zero. Overall we find that all clouds are well defined at $n = 35\,cm^{-3}$ and we can produce the most unbiased widths possible by not tweaking feature identification on a cloud-by-cloud basis.

After defining this initial $n = 35\,cm^{-3}$ threshold, we morphologically close the 3D mask by performing a dilation, followed by an erosion. This procedure removes small voids in the mask, rendering it suitable for skeletonization.[17] We then skeletonize the 3D mask using the Medial Axis Transform, convert the skeleton to a graph, and run a longest path algorithm on the resulting skeleton to obtain the main trunk of each density feature. While we only use the spine computed from the longest path algorithm to derive the widths, we also

preserve and report the full skeleton without pruning applied, in order to retain distance information on all branches. In this scheme, nearby molecular clouds can either be defined by a single, or multiple, trunks, depending on whether they are connected in density space above a threshold of $n = 35\,cm^{-3}$. Thus, this skeletonization process is performed between one and four times, depending on how many isolated 3D features there are after performing the initial thresholding. For clouds like Perseus, which manifest as a single feature in density space, we identify only a single spine. However, clouds like Taurus are actually composed of several distinct features in density space. The skeletonization and longest path algorithms are individually run on each isolated mask, to produce a set of trunks defining the cloud.[18]

Finally, we emphasize again that the FilFinder algorithm is designed to work on elongated, *filamentary* structures, with aspect ratios of at least 3:1. We find that the vast majority of our masks tend to be elongated with aspect ratios of at least 3:1, but there are a few sub-features in clouds that are better described as ellipsoids than filaments, some of which may be unresolved in the Leike et al. (2020a) map. Ellipsoids do not dominate the set of density features, either across the sample or within an individual cloud, so this has a negligible effect on the results. The volume density distributions (https://doi.org/10.7910/DVN/IADP7W), 3D masks (https://doi.org/10.7910/DVN/NMRLP1), and 3D spines (https://doi.org/10.7910/DVN/YQYBRD) are available online with full WCS information at the Harvard Dataverse. We refer interested readers there to explore our masking and skeletonization results on a cloud-by-cloud basis in more detail.

3.2. RadFil 3D

3.2.1. Building Profiles

To characterize the thicknesses of local clouds, we employ the radial profile builder RadFil (Zucker & Chen 2018a). RadFil was designed in 2D to build radial column density profiles using filament spines determined by the FilFinder package (Koch & Rosolowsky 2015; Zucker & Chen 2018a; Zucker et al. 2018a). RadFil builds profiles by taking radial cuts across the spine. The same logic for constructing a radial profile in 2D can easily be extended into 3D. We take the 3D skeleton returned by FilFinder3D, and fit a B-spline to obtain a smoothed continuous version of the spine and the first derivative along its length. Using functionality within the Python package PyVista (Sullivan & Kaszynski 2019), we generate a slice through the volume density cube at each point along the spine given the normal vector obtained from the first derivative. Then, for each point in the slice, we determine its radial distance from the spine point and its volume density via linear interpolation. On a slice-by-slice basis, we compute the median density in forty radial distance bins, spaced half a parsec apart, out to 20 pc. Given the full set of profiles, an

---

[15] Corona Australis has no significant extended density features above a level of $n = 35\,cm^{-3}$, so we skeletonize it at a level of $n = 5\,cm^{-3}$ to provide distance information. It is included in Table 1 but not in Tables 2 and 3.

[16] In previous analyses based on 2D dust emission maps (Zucker et al. 2018a), we implemented a "shift" option in the RadFil package to account for dense clumps offset from the main spine, as FilFinder does not take into the density range *inside* each mask when defining the spine. The "shift" option corrects for this by shifting each cut so that its peak density is centered at a radial distance of 0 pc. However, we forgo shifting in this work due to the small handful of noisy outliers at very high differential extinction, which would bias the density results at small radii.

[17] More details on mathematical morphology, including the erosion, dilation, and closing of features in 2D or 3D space, can be found in the scikit-image (https://scikit-image.org/) documentation, which we use to perform these operations (van der Walt et al. 2014).

[18] The two exceptions are the Musca filament and the Pipe nebula. We find that Musca is connected to the Chamaeleon cloud in 3D density space at a level of $n = 35\,cm^{-3}$. The same is true for the Pipe nebula, which is connected to Ophiuchus. Because these clouds have always been treated as individual entities in the literature, and obtaining widths for the Pipe nebula and Musca (as opposed to the Pipe-Ophiuchus, and Musca-Chamaeleon complexes) is beneficial for comparison with prior work, we mask out the Pipe nebula when obtaining widths for Ophiuchus, and the Musca cloud when obtaining widths for Chamaeleon (and vice versa). In reality, the complexes are connected by only very thin tendrils, so this procedure does not affect the morphology of the derived masks, or the resulting widths.

average profile is obtained by computing the median volume density in each radial distance bin. Before taking the average, we remove the small minority of profiles in which the peak radial density is less than the density threshold used to define the mask ($n = 35 \, \mathrm{cm}^{-3}$). For clouds composed of multiple isolated density features, the average is taken using slices across all density features, to compute a representative width for each cloud.

This averaged radial profile is used to perform the Gaussian and Plummer fitting described in Section 3.2.2. Because of the 1 pc voxel size of the 3D dust map, and the fact that Leike et al. (2020a) recommended that scales less than 2 pc are suspect, we remove the inner 2 pc of each averaged profile when fitting the profiles. However, in Appendix D, we report results for the full profile fits (including the inner 2 pc) and find that our choice to remove radial distances between 0 and 2 pc does not significantly affect our results.

3.2.2. Fitting Profiles

We fit three functions to the averaged radial volume density profile computed for each cloud in Section 3.2.1: a single-component Gaussian, a two-component Gaussian, and a Plummer function. One important consideration is the modeling of the scatter in the averaged profile. In our case, the scatter in the volume density within a bin at fixed radial distance is not a true measurement error, but rather encompasses real physical variation in the radial density profile taken at different slices along the spine of a cloud. For this reason, we choose to model the scatter on the density as part of our fitting procedure, introducing it as an additional free parameter in all three of our models. We perform our inference in a Bayesian framework, adopting a simple Gaussian likelihood (see e.g., Hogg et al. 2010) and flat priors on all our parameters. None of our parameters are prior-dominated, so this choice of flat prior has no effect on our results. For computational expediency, we minimize the negative log-likelihood, in lieu of maximizing the likelihood. Our Gaussian log-likelihood is of the form

$$\ln p(n \mid \theta, \sigma_n^2) = -\frac{1}{2} \sum_i \left[\frac{[n_i - n_{\theta,i}]^2}{\sigma_n^2} + \ln(2\pi\sigma_n^2) \right] \quad (1)$$

where n_i is the measured density in the ith radial distance bin, $n_{\theta,i}$ is the modeled density in the ith radial distance bin (defined by the free parameters θ), and σ_n^2 is the square of the scatter in the density across all bins that we also infer as part of our modeling.

For the single-component Gaussian fit, our model for the volume density of hydrogen nuclei n as a function of radial distance r is of the form

$$n(r) = a \exp\left(\frac{-r^2}{2\sigma^2}\right). \quad (2)$$

Our free parameters θ are the amplitude (a) and standard deviation (σ). The mean of the Gaussian is fixed to zero. We adopt a flat prior between 0 and 80 cm^{-3} for a, between 0 and 15 pc for σ, and between 0 and 100 cm^{-3} for σ_n^2.

To better model the significant tails of the distribution, we additionally fit a two-component Gaussian, again with the mean of each component fixed to zero:

$$n(r) = a_1 \exp\left(\frac{-r^2}{2\sigma_1^2}\right) + a_2 \exp\left(\frac{-r^2}{2\sigma_2^2}\right) \quad (3)$$

where the amplitudes (a_1, a_2) and their standard deviations (σ_1, σ_2) are the free parameters in the modeling. We adopt a flat prior between 20 and 80 cm^{-3} for a_1, between 0 and 6 pc for σ_1, between 2 and 20 cm^{-3} for a_2, between 6 and 25 pc for σ_2, and between 0 and 100 cm^{-3} for σ_n^2. The offset in the prior range between a_1 and a_2 is adopted to avoid degeneracies in the modeling.

Finally, we fit a Plummer function, which we parameterize as

$$n(r) = \frac{n_0}{\left[1 + \left(\frac{r}{R_{\mathrm{flat}}}\right)^2 \right]^{\frac{p}{2}}} \quad (4)$$

where our free parameters are n_0 (peak profile height), R_{flat} (the flattening radius), and p (index of the density profile). Equation (4) is the same ubiquitous Plummer function applied to column density maps of smaller-scale filaments (widths a few tenths of a parsec, lengths a few parsecs; Panopoulou et al. 2017; Arzoumanian et al. 2019) from the Herschel Gould Belt Survey (André et al. 2010), except we have transformed the model from column density space back to volume density space (see Equation (1) of Arzoumanian et al. 2011). We adopt a flat prior between 20 and 170 cm^{-3} for n_0, between 0 and 15 pc for R_{flat}, between 0 and 6 for p, and between 0 and 100 cm^{-3} for σ_n^2.

We sample for all model parameters using the nested sampling code `dynesty` (Speagle 2020). We adopt the default parameters of the nested sampler, with a stopping criterion of `dlogz = 0.1`. We utilize the logarithm of the evidence $\ln(Z)$ extracted from the `dynesty` chains to compute a Bayes Factor for the purpose of model comparison, as discussed further in Section 4.

3.3. Creating 2D Dust Extinction Maps from 3D Dust Data

To compare the Leike et al. (2020a) 3D dust map with traditional 2D approaches (see Section 2.2), we create projected 2D dust extinction maps from the 3D volume density distributions used in the construction of the radial profiles. To do so, we utilize the `FitsOffAxisProjection` functionality from the Python package `yt` (Turk et al. 2011). The `FITSOffAxisProjection` function integrates the volume density n along a line of sight $\hat{l}$, where $\hat{l}$ is determined by the vector between the Sun and the median cartesian coordinates of the points in a cloud's skeleton, (x_{cen}, y_{cen}, z_{cen}). The resulting projection corresponds to the total hydrogen column density distribution $N = N_{\mathrm{H\,I}} + 2N_{\mathrm{H_2}}$ (in cm^{-2}) as seen from the Sun. In order to compare with the NICEST maps of the K-band extinction A_K (from Section 2.2), we convert from total hydrogen column density to A_K by assuming a constant conversion factor from Lada et al. (2009) of $\frac{N(\mathrm{H\,I}) + 2N(\mathrm{H_2})}{A_K} = 1.67 \times 10^{22} \, \mathrm{cm}^{-2} \, \mathrm{mag}^{-1}$.

To assign sky coordinates to each projection, we convert from the skeleton's central coordinates (x_{cen}, y_{cen}, z_{cen}) to sky coordinates (l_{cen}, b_{cen}, d_{cen}), where l_{cen} and b_{cen} become the central Galactic Longitude and Latitude of the projected image

Table 1
Skeletonization Results

Cloud (1)	l (°) (2)	b (°) (3)	d_{min} (pc) (4)	d_{med} (pc) (5)	d_{max} (pc) (6)	x_{min} (pc) (7)	x_{max} (pc) (8)	y_{min} (pc) (9)	y_{max} (pc) (10)	z_{min} (pc) (11)	z_{max} (pc) (12)	$N_{components}$ (13)	$l_{skeleton}$ (pc) (14)
Chamaeleon	299.0	−15.9	173	183	190	69	99	−159	−148	−57	−35	1	68
Ophiuchus	355.4	17.0	115	136	150	104	144	−26	5	24	48	3	74
Lupus	341.7	5.1	155	165	198	139	196	−73	−28	4	47	3	80
Taurus	172.6	−15.6	131	148	168	−166	−122	6	44	−45	−26	3	79
Perseus	158.9	−20.2	279	295	301	−270	−236	95	100	−116	−81	1	57
Musca	301.0	−9.7	171	172	173	86	91	−146	−145	−36	−22	1	16
Pipe	2.1	4.1	147	152	163	146	163	−8	7	6	18	1	27
Cepheus	112.1	15.9	337	345	370	−133	−65	300	323	81	133	4	52
Corona Australis[a]	6.5	−24.6	136	161	179	132	162	−2	24	−77	−33	1	86
Orion A[b]	212.5	−19.6	391	405	445	−349	−315	−241	−177	−149	−118	3	52
Orion B[b]	205.5	−14.0	397	404	406	−362	−332	−190	−157	−114	−76	1	69
λ Orionis[b]	194.3	−14.6	375	386	397	−367	−356	−129	−73	−109	−73	3	62

Notes. Properties of the 3D skeletons for local molecular clouds. (1) Name of the cloud. (2–3) Median Galactic longitude l and latitude b of the points defining the cloud's skeleton. (4–6) Minimum, median, and maximum distance of the points defining the skeleton. (7–8) Minimum and maximum extent of the cloud's skeleton in the Heliocentric Galactic cartesian x direction. (9–10) Minimum and maximum extent of the cloud's skeleton in the Heliocentric Galactic cartesian y direction. (11–12) Minimum and maximum extent of the cloud's skeleton in the Heliocentric Galactic cartesian z direction. (13) Number of skeletons per cloud, determined by the number of significant features above a density threshold of $n = 35$ cm^{-3}. (14) Total length of the set of skeletons in (13), computed using only each skeleton's main trunk via FilFinder's longest path algorithm. At the Harvard Dataverse (https://doi.org/10.7910/DVN/YQYBRD), we provide tables in FITS format with the (x, y, z, l, b, d) values of each point in the spine (for both the longest path skeleton summarized here and the full, unpruned skeleton). We also provide a machine readable version of this table (see https://doi.org/10.7910/DVN/CAVMAQ). Interactive figures highlighting these skeletonization results are available at https://faun.rc.fas.harvard.edu/czucker/Paper_Figures/3D_Cloud_Topologies/gallery.html or in the online version of the published article.
[a] Corona Australis is too diffuse to meet the minimum density threshold to be included in the width analysis for this study. We skeletonize the cloud at a much lower threshold ($n = 5$ cm^{-3}) to provide distance information, but do not include it in subsequent analysis in Tables 2 and 3.
[b] Clouds below the horizontal line—Orion A, Orion B, and λ Orionis—should be treated with caution, as they lie at the very edge of the Leike et al. (2020a) 3D dust grid and are subjected to additional biases. Part of Orion A, toward the Orion Nebula Cluster, is also devoid of dust in the Leike et al. (2020a) 3D dust map despite being highly extinguished. See Section 5 for full details.

on the plane of the sky, and d_{cen} is the distance between the Sun and the central point of the cloud's skeleton. The pixel scale of the image is computed by determining the angular size spanned by a 1 pc voxel (the voxel size of the original 3D dust grid) at the central distance of the cloud's skeleton d_{cen}. These projected A_K maps are available for download at the Harvard Dataverse (see https://doi.org/10.7910/DVN/GXXKHD).

3.4. Mass Calculation

To quantify the fraction of cloud mass being recovered with 3D dust mapping, we compute cloud masses using both traditional NICEST 2D dust extinction maps (from Section 2.2) and the projected A_K maps we derive from the 3D dust in Section 3.3. In both cases, we adopt a consistent threshold of $A_K = 0.1$ mag. This threshold is the same used in previous literature to calculate cloud masses from the NICEST 2D dust extinction maps (see e.g., Lada et al. 2010).[19] The masses are calculated inside the cloud boundaries by assuming the same mass surface density relation as Zari et al. (2016). This relation is equivalent to $\frac{\Sigma_{gas}}{A_K} = \mu m_p \beta_K = 183\ M_\odot$ pc^{-2} mag^{-1}, where $\mu = 1.37$ is the mean molecular weight, $m_p = 1.67 \times 10^{-24}$ g is the mass of the proton, and β_K is the same gas-to-dust ratio that

we adopt above, equivalent to 1.67×10^{22} cm^{-2} mag^{-1}. To ensure a fair comparison, the NICEST maps from Section 2.2 are convolved to the same resolution as the Leike et al. (2020a) based extinction maps. In both cases, the same distance d_{cen}—the average distance to a cloud's skeleton—is adopted.

4. Results

4.1. Skeletonization

In Table 1 we summarize the properties of the skeletons, determined using FilFinder3D's longest path algorithm, for all clouds in our sample. This includes the minimum, median, and maximum distance to each cloud's skeleton, along with the extent of the cloud's skeleton along the Heliocentric Galactic cartesian x, y, and z directions. We also include the number of skeletal components (skeletonized at a density threshold above $n = 35$ cm^{-3}) and the total length of these components. The length is the total length of *denser* features (computed using only the skeleton returned by the longest path algorithm) so it does not include features branching off the main trunk. The properties of both the longest path skeletons, and the full unpruned skeletons, are available online in machine readable format on the Harvard Dataverse (see https://doi.org/10.7910/DVN/YQYBRD). The skeletonization results for two clouds (Perseus and Chamaeleon) are shown in Figures 1 and 2, respectively. These figures are interactive in their online version; it is possible to manipulate the skeleton in 3D, or hover over any point in the 2D skeleton to obtain its plane-of-the-sky coordinates and distance. Comparable interactive figures for the rest of the clouds in the sample are available
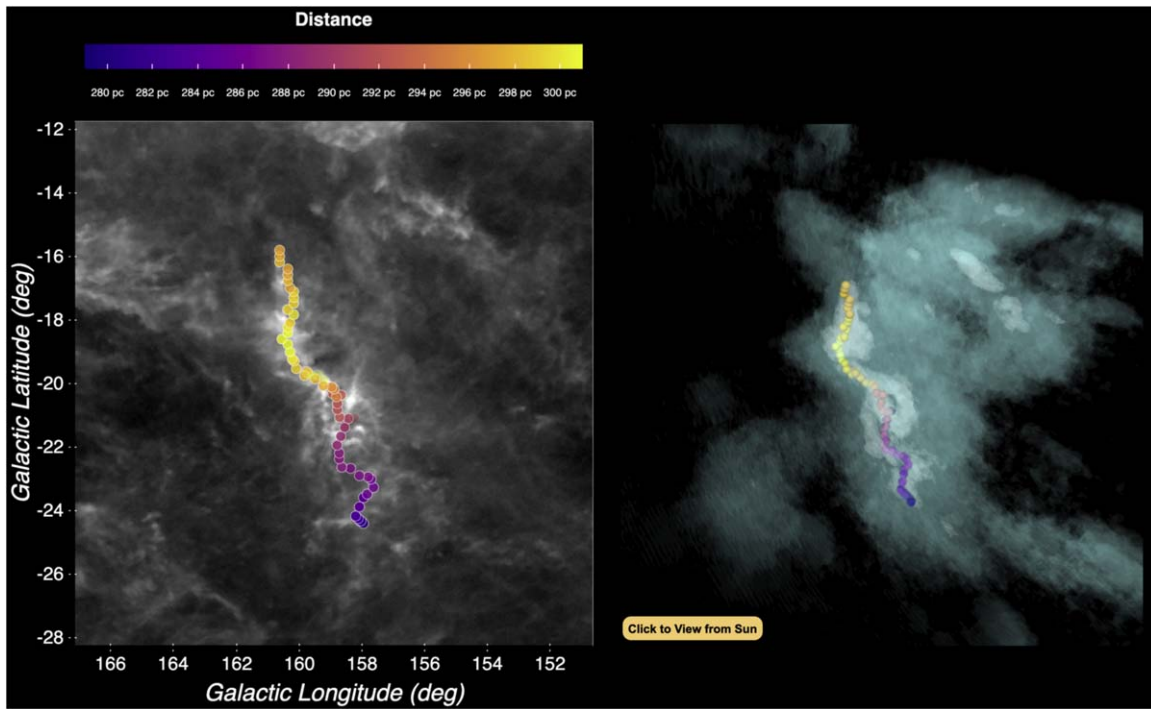
---

[19] Like Lada et al. (2010), we also subtract a constant background of $A_K = 0.15$ mag from the Pipe nebula, due to its position close to the plane and toward the Galactic center. Furthermore, because the 2D dust extinction maps based on Leike et al. (2020a) are computed using only dust local to the cloud, rather than integrated along the line of sight, we limit our comparison to latitudes $|b| > 5°$. In reality, this latitude cut only masks out a small section of the Pipe and Lupus clouds.

Figure 1. Skeletonization results for the Perseus Molecular Cloud shown in 2D (left panel) and 3D (right panel). In both panels, the scatter points (colored by distance over the range $d = 279$–301 pc) delineate the skeleton of the cloud, determined in 3D Cartesian space and projected back on the plane of the sky. In the 3D version of the figure we show the 3D volume density of the cloud n, where the cyan and white distributions indicate lower thresholds of $n = 4$ cm^{-3} and $n = 35$ cm^{-3}, respectively. In the plane of the sky version, we show the Planck reddening map (Planck Collaboration et al. 2011). An interactive version of this figure is available at https://faun.rc.fas.harvard.edu/czucker/Paper_Figures/3D_Cloud_Topologies/perseus_topology/perseus.html or in the online version of the published article. Comparable interactive figures for all clouds in the sample are available at https://faun.rc.fas.harvard.edu/czucker/Paper_Figures/3D_Cloud_Topologies/gallery. html. In the online version, the cyan and white boundaries (toggleable on/off) correspond to the FWHM of the inner and outer envelopes of the cloud, derived from the two-component Gaussian fitting results in Section 4.

at https://faun.rc.fas.harvard.edu/czucker/Paper_Figures/3D_Cloud_Topologies/gallery.html or in the online version of the published article.

We have separated Table 1 into two parts, representing "complete" (top rows) and "incomplete" (bottom rows) clouds. Incomplete clouds—Orion A, Orion B, and λ Orionis—are those that lie at the very edge of the Leike et al. (2020a) 3D dust map, which extends to 370 pc along the cartesian x and y directions. While these three clouds are still capable of being skeletonized, it is likely that some fraction of each cloud lies beyond the map boundary, which would bias the skeletons to be mildly closer in distance than they actually are. This incompleteness will be further validated in Section 4.4, where projected 2D extinction maps based on the Leike et al. (2020a) 3D dust distribution indicate that Orion A, Orion B, and λ Orionis are the only three clouds in the sample whose masses are significantly discrepant from counterpart masses calculated out to "infinity" (that is, using the NICEST algorithm; Lombardi 2009). This discrepancy indicates that there is missing mass present beyond the boundaries of the map.

4.2. Width Results

In Table 2, we summarize the results of our radial volume density fitting procedure. A machine readable version of Table 2 is available at the Harvard Dataverse (https://doi.org/10.7910/DVN/QKYR3G). For each cloud and fit (two-component Gaussian, Plummer, single-component Gaussian) we list the average and 1σ uncertainty on each parameter. In each case, we obtain a set of samples derived from the

dynesty nested sampling procedure. The average value reported is the median (50th percentile) of the samples. The upper and lower bounds are the difference between the 50th and 84th percentiles of the samples, and the 16th and 50th percentiles of the samples, respectively. Cornerplots showing the marginalized posterior distributions for each cloud and type of fit are available online at the Harvard Dataverse (https://doi.org/10.7910/DVN/YVQC7X). The radial volume density profiles for two clouds—Perseus and Chamaeleon—are shown in Figure 3, and similar figures are available for the rest of the clouds in Appendix A. The data behind these figures, including both the median and full ensemble of radial profiles computed for each cloud, are available at the Harvard Dataverse (see https://doi.org/10.7910/DVN/JBRWHB).

We summarize the width results in Figures 4 and 5. We exclude the single-component Gaussian from the summary due to its poor Bayes Factor relative to the two-component Gaussian and Plummer profiles (as justified in Section 4.2.1). Figure 4 shows a cornerplot of the best-fit results for the two-component Gaussian model parameters, while Figure 5 shows a cornerplot of the best-fit results for the Plummer model parameters. We find that for our two-component Gaussian results, inner widths σ_1 span 2.5–4.9 pc, with an average of ≈ 3.0 pc. The outer widths span 8 and 18 pc, with an average of ≈ 11 pc. We find a relatively tight spread in the ratio of the widths of the outer to inner envelopes ($\frac{\sigma_2}{\sigma_1}$), with an average value of 3.4 and a scatter of only 0.9. The amplitude a_1 of the inner Gaussian spans $n = 25$–53 cm^{-3}, about three times as large as the amplitude a_2 of the outer Gaussian, which spans $n = 5$ to 15 cm^{-3}. The widths of our Plummer fits R_{flat} span 1.2-8.1 pc
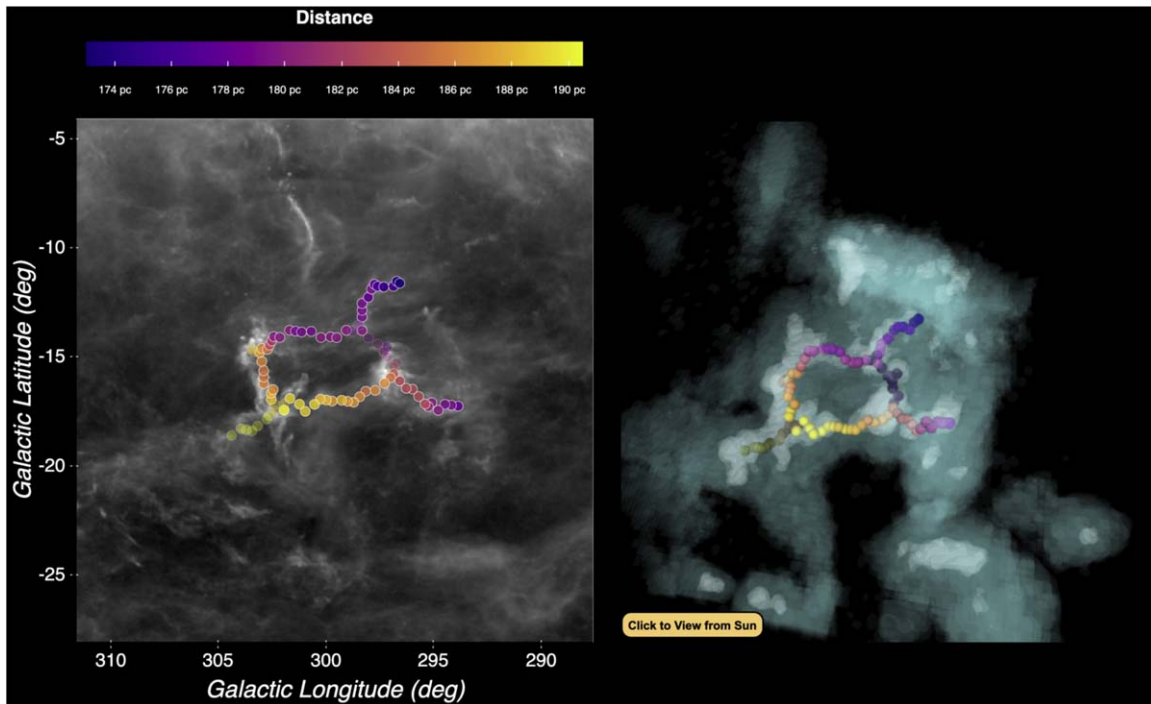
Figure 2. Same as in Figure 1 but for the Chamaeleon Molecular Cloud, with the spine (colored points) spanning a distance range of $d = 173$–190 pc. Opaque spine points constitute the skeleton's main spine, while semi-transparent points are part of the full, unpruned skeleton. An interactive version of this figure is available at https://faun.rc.fas.harvard.edu/czucker/Paper_Figures/3D_Cloud_Topologies/chamaeleon_topology/chamaeleon.html or in the online version of the published article. Comparable interactive figures for all clouds in the sample are available at https://faun.rc.fas.harvard.edu/czucker/Paper_Figures/3D_Cloud_Topologies/gallery.html.

with a typical value of $R_{flat} = 3.6$ pc. The power-law indices p of the Plummer fit range from 1.2 and 3.4, with a median value of 1.8. The peak density parameter n_0 ranges from 35 to 117 cm^{-3}, with a median of 49 cm^{-3}. When the inner 2 pc of the profile is excluded, the Plummer fits often have a higher value of n_0 than measured, suggesting, as we will argue in Section 6, that much of the densest structure in the 3D dust map is unresolved.

4.2.1. Model Comparison

In addition to the best-fit parameters, we evaluate the performance of the models in light of the data. From Bayes' Theorem the posterior probability of a model $\mathcal{M}$ given the data $\mathcal{D}$ is proportional to

$$p(\mathcal{M}|\mathcal{D}) \propto p(\mathcal{D}|\mathcal{M})p(\mathcal{M}) \quad (5)$$

where $p(\mathcal{D}|\mathcal{M})$ is the likelihood of the data given the model and $p(\mathcal{M})$ is the prior probability of the model. To directly compare two models, $\mathcal{M}_1$ versus $\mathcal{M}_2$, we are interested in the ratio of their posterior probabilities (or posterior odds), given as

$$\frac{p(\mathcal{M}_1|\mathcal{D})}{p(\mathcal{M}_2|\mathcal{D})} = B_{12}\frac{p(\mathcal{M}_1)}{p(\mathcal{M}_2)} \quad (6)$$

with the Bayes Factor, $\mathcal{B}_{12}$, equal to the ratio of the marginal likelihood (also known as the evidence $\mathcal{Z}$) of the two models:

$$B_{12} = \frac{p(\mathcal{D}|\mathcal{M}_1)}{p(\mathcal{D}|\mathcal{M}_2)} = \frac{\mathcal{Z}_1}{\mathcal{Z}_2}. \quad (7)$$

Assuming equal prior odds ($\frac{p(\mathcal{M}_1)}{p(\mathcal{M}_2)} = 1$), the posterior odds is simply the Bayes Factor. The logarithm of the evidence $\ln(\mathcal{Z})$ is conveniently returned for each model fit by the nested sampling package `dynesty` and is summarized in Table 2.

The logarithm of the Bayes Factor is then given as

$$\ln(\mathcal{B}_{12}) = \ln(\mathcal{Z}_1) - \ln(\mathcal{Z}_2). \quad (8)$$

Computing $\ln(\mathcal{B}_{12})$ for the two-component Gaussian and Plummer Models, respectively, with regards to the single-component Gaussian model, we find that the two-component Gaussian has on average $\ln(\mathcal{B}_{12}) = 44$ over the single-component Gaussian, whereas the Plummer model has on average $\ln(\mathcal{B}_{12}) = 39$ over the single-component Gaussian. Based on the empirical "Jeffrey's" scale for evaluating the relative strength of two models (Jeffreys 1939), $\ln(\mathcal{B}_{12}) > 5$ represents decisive evidence in favor of a given model. Because the Bayes Factor has a built in penalty for model complexity, the decisive evidence in favor of the two-component Gaussian and Plummer models is not due to the increased parameterization of the fit. Based on these Bayes Factor calculation, we can conclude that the single-component Gaussian fit is heavily disfavored with respect to both the two-component and Plummer fits. When comparing $\ln(\mathcal{B}_{12})$ for the two-component Gaussian and Plummer models, we find that the Plummer is decisively favored for two clouds, while the two-component Gaussian is decisively favored for four clouds, with the remaining clouds only having moderate evidence in favor of either model. Ruling out the single-component Gaussian model, we will discuss the theoretical implications of both the two-component Gaussian and Plummer profiles in Section 6.

4.3. Potential Additional Sources of Fitting Uncertainty

While the formal uncertainties on all parameters are reported in Table 2, there are potential additional systematic effects, which we discuss here.

Table 2
Radial Volume Density Fitting Results

Cloud	Two-component Gaussian							Plummer					Single Gaussian			
	σ_1 (pc)	a_1 (cm^{-3})	σ_2 (pc)	a_2 (cm^{-3})	$\sigma^2_{n,\mathrm{G2}}$ (cm^{-3})	$\frac{\sigma_2}{\sigma_1}$	$\ln Z_{\mathrm{G2}}$	n_0 (cm^{-3})	R_{flat} (pc)	p	$\sigma^2_{n,\mathrm{P}}$ (cm^{-3})	lnZ_P	σ (pc)	a (cm^{-3})	$\sigma^2_{n,\mathrm{G1}}$ (cm^{-3})	$\ln Z_{\mathrm{G1}}$
(1)	(2)	(3)	(4)	(5)	(6)	(7)	(8)	(9)	(10)	(11)	(12)	(13)	(14)	(15)	(16)	(17)
Chamaeleon	$2.9^{+0.1}_{-0.1}$	$31.3^{+0.5}_{-0.6}$	$10.2^{+0.4}_{-0.3}$	$8.7^{+0.5}_{-0.5}$	$0.2^{+0.0}_{-0.0}$	3.5	-2.9	$47.8^{+1.5}_{-1.2}$	$3.1^{+0.1}_{-0.2}$	$1.8^{+0.1}_{-0.1}$	$0.1^{+0.0}_{-0.0}$	-1.5	$4.8^{+0.3}_{-0.3}$	$30.8^{+2.1}_{-2.0}$	$6.1^{+1.9}_{-1.3}$	-58.0
Ophiuchus	$2.7^{+0.2}_{-0.2}$	$31.1^{+1.6}_{-1.5}$	$10.1^{+0.6}_{-0.5}$	$12.6^{+1.1}_{-1.1}$	$0.8^{+0.2}_{-0.2}$	3.8	-27.2	$56.0^{+3.5}_{-2.9}$	$2.3^{+0.2}_{-0.2}$	$1.4^{+0.0}_{-0.0}$	$0.3^{+0.1}_{-0.1}$	-11.9	$5.8^{+0.5}_{-0.4}$	$29.1^{+2.0}_{-2.0}$	$9.5^{+2.6}_{-2.0}$	-64.7
Lupus	$2.6^{+0.3}_{-0.2}$	$30.6^{+1.8}_{-1.8}$	$8.1^{+0.6}_{-0.5}$	$15.5^{+1.9}_{-2.0}$	$0.9^{+0.3}_{-0.2}$	3.1	-29.2	$48.6^{+2.3}_{-1.9}$	$3.6^{+0.3}_{-0.3}$	$1.9^{+0.1}_{-0.1}$	$0.5^{+0.1}_{-0.1}$	-19.3	$5.2^{+0.3}_{-0.3}$	$32.7^{+1.8}_{-1.7}$	$6.2^{+1.7}_{-1.3}$	-58.1
Taurus	$2.6^{+0.1}_{-0.1}$	$30.9^{+1.2}_{-1.1}$	$11.9^{+0.6}_{-0.5}$	$9.2^{+0.5}_{-0.5}$	$0.4^{+0.1}_{-0.1}$	4.6	-17.4	$72.8^{+22.7}_{-11.1}$	$1.2^{+0.3}_{-0.3}$	$1.2^{+0.0}_{-0.0}$	$0.4^{+0.1}_{-0.1}$	-17.3	$5.8^{+0.6}_{-0.6}$	$24.3^{+2.4}_{-2.2}$	$10.3^{+3.3}_{-2.3}$	-65.7
Perseus	$4.1^{+0.1}_{-0.1}$	$34.3^{+0.9}_{-0.9}$	$11.9^{+0.8}_{-0.6}$	$10.9^{+1.0}_{-1.0}$	$0.3^{+0.1}_{-0.1}$	2.9	-15.0	$47.8^{+0.9}_{-0.9}$	$6.1^{+0.3}_{-0.3}$	$2.4^{+0.1}_{-0.1}$	$0.5^{+0.1}_{-0.1}$	-20.7	$6.0^{+0.2}_{-0.2}$	$39.0^{+2.1}_{-1.5}$	$6.9^{+2.1}_{-1.4}$	-60.4
Musca[a]	$3.1^{+0.1}_{-0.1}$	$31.8^{+1.5}_{-1.5}$	$17.9^{+4.1}_{-3.0}$	$4.9^{+0.7}_{-0.6}$	$1.3^{+0.4}_{-0.3}$	5.8	-34.4	$48.3^{+8.4}_{-5.5}$	$2.5^{+0.6}_{-0.5}$	$1.6^{+0.2}_{-0.2}$	$2.4^{+0.7}_{-0.5}$	-44.5	$4.4^{+0.4}_{-0.4}$	$29.8^{+3.0}_{-2.9}$	$8.9^{+2.7}_{-2.0}$	-63.8
Pipe	$4.1^{+0.4}_{-0.4}$	$25.5^{+2.7}_{-2.8}$	$9.7^{+2.5}_{-1.2}$	$9.0^{+3.3}_{-3.4}$	$1.5^{+0.5}_{-0.3}$	2.4	-36.7	$35.5^{+1.5}_{-1.4}$	$7.7^{+1.2}_{-1.0}$	$3.4^{+0.6}_{-0.5}$	$1.4^{+0.4}_{-0.3}$	-35.5	$5.7^{+0.2}_{-0.2}$	$30.6^{+1.2}_{-1.1}$	$3.5^{+1.1}_{-0.7}$	-49.3
Cepheus	$2.5^{+0.1}_{-0.1}$	$46.6^{+1.7}_{-1.6}$	$10.9^{+0.7}_{-0.7}$	$10.1^{+0.7}_{-0.7}$	$0.7^{+0.2}_{-0.2}$	4.4	-26.4	$116.9^{+23.7}_{-17.5}$	$1.3^{+0.2}_{-0.2}$	$1.4^{+0.0}_{-0.0}$	$0.5^{+0.2}_{-0.1}$	-21.6	$4.3^{+0.4}_{-0.4}$	$39.1^{+3.9}_{-3.7}$	$14.3^{+4.2}_{-3.0}$	-71.4
Orion A[b]	$2.9^{+0.1}_{-0.1}$	$52.4^{+1.8}_{-1.8}$	$8.4^{+1.0}_{-0.8}$	$8.8^{+1.9}_{-1.7}$	$1.3^{+0.4}_{-0.3}$	2.9	-35.0	$68.3^{+3.4}_{-3.0}$	$4.4^{+0.5}_{-0.4}$	$3.1^{+0.3}_{-0.3}$	$1.5^{+0.5}_{-0.3}$	-37.2	$3.7^{+0.1}_{-0.1}$	$53.1^{+2.5}_{-2.4}$	$5.8^{+1.8}_{-1.3}$	-57.5
Orion B[b]	$4.9^{+0.1}_{-0.1}$	$39.2^{+1.1}_{-1.1}$	$14.6^{+1.9}_{-1.3}$	$9.0^{+1.3}_{-1.2}$	$0.3^{+0.1}_{-0.1}$	3.0	-13.6	$50.3^{+0.8}_{-0.8}$	$8.1^{+0.5}_{-0.4}$	$3.0^{+0.2}_{-0.2}$	$0.6^{+0.2}_{-0.1}$	-23.6	$6.5^{+0.2}_{-0.2}$	$43.8^{+1.4}_{-1.3}$	$5.9^{+1.8}_{-1.2}$	-58.0
λ Orionis[b]	$3.7^{+0.1}_{-0.1}$	$27.2^{+0.5}_{-0.5}$	$12.8^{+0.5}_{-0.4}$	$9.3^{+0.4}_{-0.4}$	$0.1^{+0.0}_{-0.0}$	3.4	-0.7	$40.2^{+1.1}_{-1.0}$	$4.3^{+0.3}_{-0.3}$	$1.7^{+0.1}_{-0.1}$	$0.3^{+0.1}_{-0.1}$	-14.0	$6.3^{+0.3}_{-0.4}$	$29.1^{+1.6}_{-1.6}$	$7.2^{+2.0}_{-1.5}$	-60.2

Notes. Cloud thickness results, obtained via radial volume density profile fitting of each cloud's 3D density distribution. (1) Name of the cloud. (2–6) Best-fit parameters for the two-component Gaussian fit, including the standard deviation and amplitude of the narrower Gaussian (σ_1, a_1), the standard deviation and amplitude of the broader Gaussian (σ_2, a_2), and the square of the modeled scatter in the density measurements ($\sigma^2_{n,\mathrm{G2}}$). (7) Ratio of the outer to inner Gaussian standard deviations. (8) Logarithm of the evidence of the two-component Gaussian fit. (9–12) Best-fit parameters of the Plummer fit, including the peak amplitude n_0, the flattening radius R_{flat}, the power index of the density profile p, and the square of the modeled scatter in the density measurements ($\sigma^2_{n,\mathrm{P}}$). (13) Logarithm of the evidence of the Plummer fit. (14–16) Standard deviation σ, amplitude a, and the square of the modeled scatter in the density measurements ($\sigma^2_{n,\mathrm{G1}}$) for the single-component Gaussian fit. (17) Logarithm of the evidence of the single-component Gaussian fit. We report the single-component Gaussian results here for completeness only, as it is a poor fit to the data particularly at large radial distances. A machine readable version of this table is available at https://doi.org/10.7910/DVN/QKYR3G.
[a] At small radial distances, Musca is largely unresolved in the Leike et al. (2020a) map, and at large radial distances, its structure is consistent with being prior-dominated, so we urge caution when interpreting the results.
[b] Clouds below the horizontal line—Orion A, Orion B, and λ Orionis—should be treated with caution, as they lie at the very edge of the Leike et al. (2020a) 3D dust grid and are subjected to additional biases. Part of Orion A, toward the Orion Nebula Cluster, is also devoid of dust in the Leike et al. (2020a) 3D dust map despite being highly extinguished. See Section 5 for full details.
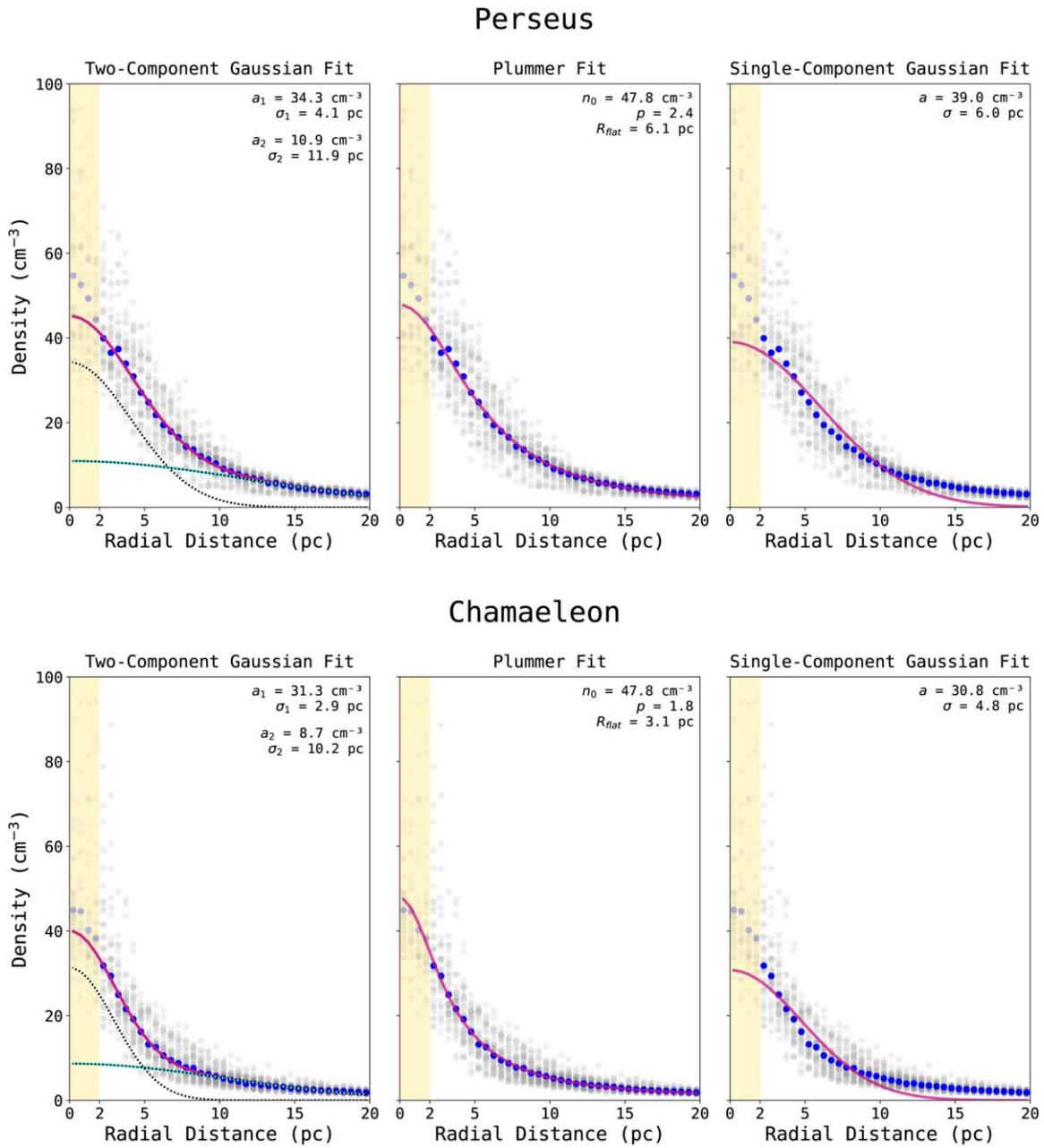
Perseus

Chamaeleon

Figure 3. Radial volume density profile for the Perseus Molecular Cloud (top row) and the Chamaeleon Molecular Cloud (bottom row). Because the Leike et al. (2020a) 3D dust map is more reliable at scales >2 pc and is not capable of probing the highest gas densities, we exclude the inner 2 pc (coincident with the yellow bar) from the fit. In each panel the gray dots indicate the profiles for individual slices along the spine, while the blue dots indicate the median of all slices. We fit three functions to the averaged radial volume density profile, whose fits are shown in solid red: a two-component Gaussian function (left panels), a Plummer function (middle panels), and a single-component Gaussian function (right panels). In the left panels, we additionally overlay the decomposition of the two Gaussians via the dashed white and cyan lines, corresponding to the "inner" (black–white dotted) and "outer" (black–cyan dotted) components. Identical plots for the rest of the sample are available in Appendix A.

4.3.1. Degeneracy of the Plummer Profile

While the Bayes Factor indicates that the Plummer function is sometimes preferred over the two-component Gaussian function, there are clear caveats to using a Plummer fit that should not go unmentioned. In particular, it is well known—both from observations and simulations—that two parameters in the Plummer function—p and R_{flat} are *highly* degenerate. We see this trend clearly in Figure 5, where p and R_{flat} are strongly correlated. In particular, as R_{flat} increases so does the value of p. This covariance has also been shown in synthetic filaments on much smaller scales (lengths ≈a few parsecs, widths ≈a few tenths of a parsec) in

AREPO simulations from Smith et al. (2014), where the Plummer function was fit to the radial *column* density distribution. We likewise see this in observations of the radial column density distributions of large-scale filaments (lengths ≈tens of parsecs, widths ≈1 pc; Zucker et al. 2018a), where p and R_{flat} show strong correlation. Accordingly, we urge caution when interpreting the Plummer profiles, as discussed in Section 6.2.

4.3.2. Intra-cut Variation in the Radial Profiles

In producing the averaged radial profile for fitting, we are not explicitly taking into account the variation in the radial profiles along the spine of each cloud. To summarize the variation, we have
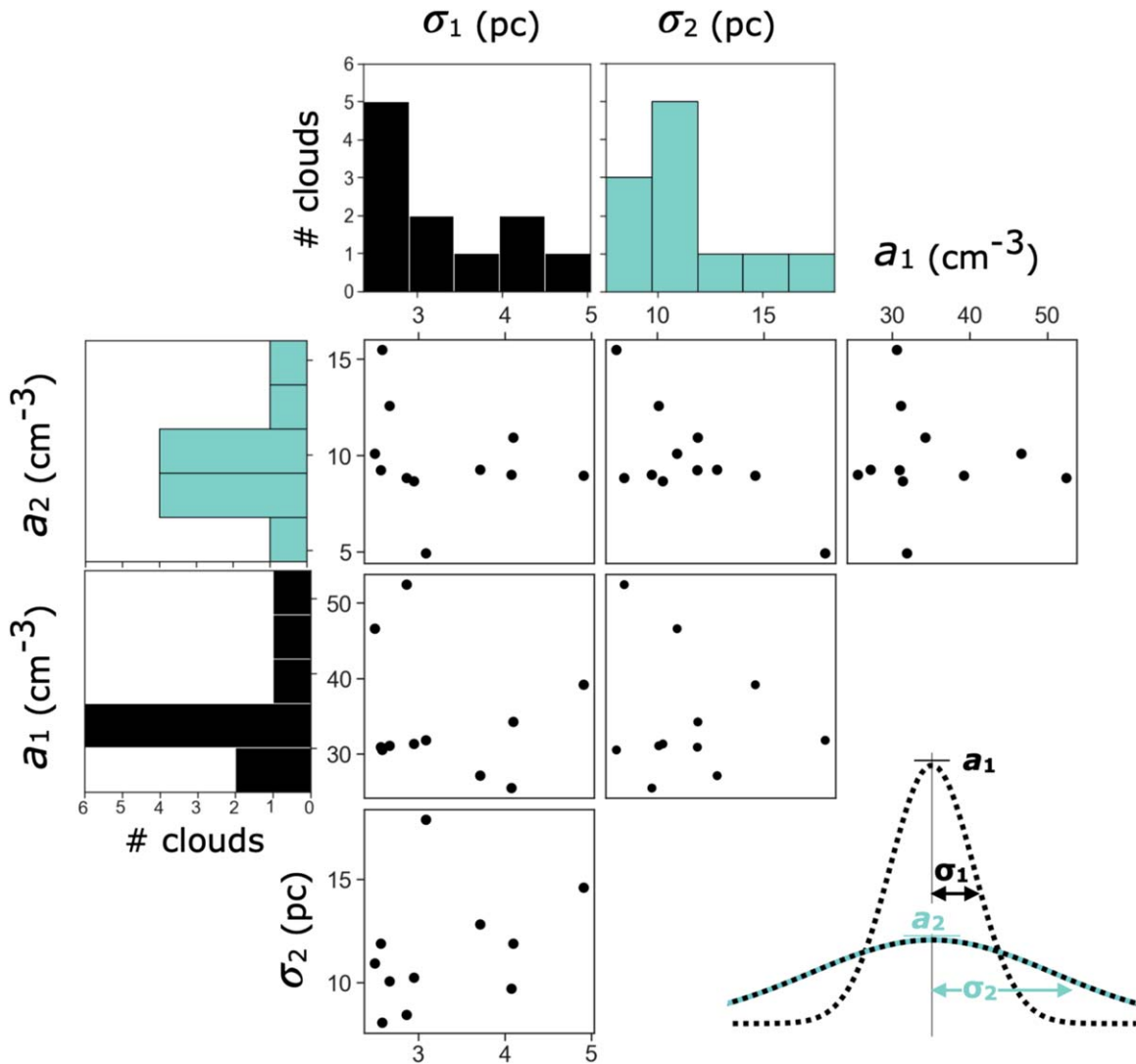
Figure 4. Summary of the radial volume density profile fitting results for the two-component Gaussian function, including the standard deviation σ_1 of the inner Gaussian, the standard deviation σ_2 of the outer Gaussian, the amplitude of the inner Gaussian a_1, and the amplitude of the outer Gaussian a_2. Each point represents a single local cloud in the sample.

chosen to model the variable σ_n^2, which represents the scatter in the density profile values, capturing how much variation in the density we observe in a radial distance bin across all cuts. In general, for our better-fitting models (Plummer and two-component Gaussian), we find that our fits prefer a small value for σ_n^2, equivalent to a few particles per cubic centimeter in density n. This trend is also evident in Figures 1 and 2. We do see a large scatter from cut to cut at small radial distances ($r < 2$ pc), but these distances are excluded from the fit. For the remainder of the profile the scatter is significantly reduced, and is likely driving the low inferred value for σ_n^2. From this, we conclude that while inter-cut variation in the radial volume density profile may have some modest affect on our inferred value for the inner width σ_1 of the two-component Gaussian, it likely has less effect on the outer width σ_2 of the two-component Gaussian or the R_{flat} of our Plummer fits.

4.3.3. Bias in Derived Widths as a Function of Cloud Distance

In order to confirm that we are probing intrinsic variation in the cloud widths, rather than the resolution of the underlying 3D dust map, it is necessary to verify that our derived cloud widths are *not*

dependent on the distance of the cloud. If this dependence exists, we expect clouds at larger distances to have larger widths, due to degradation in the quality of Gaia parallax measurements underpinning the Leike et al. (2020a) 3D dust map at larger distances. To examine this potential correlation, we plot all width parameters in Table 2 as a function of cloud distance, which we show in Appendix B and Figure B1. We find no correlation between cloud distance and cloud width for any width parameter, suggesting that our properties are being driven by the intrinsic widths of clouds, rather than by distance biases.

4.3.4. Including the Inner 2 pc of the Radial Profiles when Fitting

In Section 4, we report results where radial distances between 0 and 2 pc (closest to the spine) are excluded from the radial profiles, due to combination of the 3D dust map's 1 pc voxel width and the caveat from Leike et al. (2020a) that scales less than 2 pc are unreliable. To ensure that our choice to exclude the inner 2 pc does not significantly affect our results, we refit the radial profiles using all radial distances between 0 and 20 pc, and those results are reported in Appendix D. Overall, we find that including
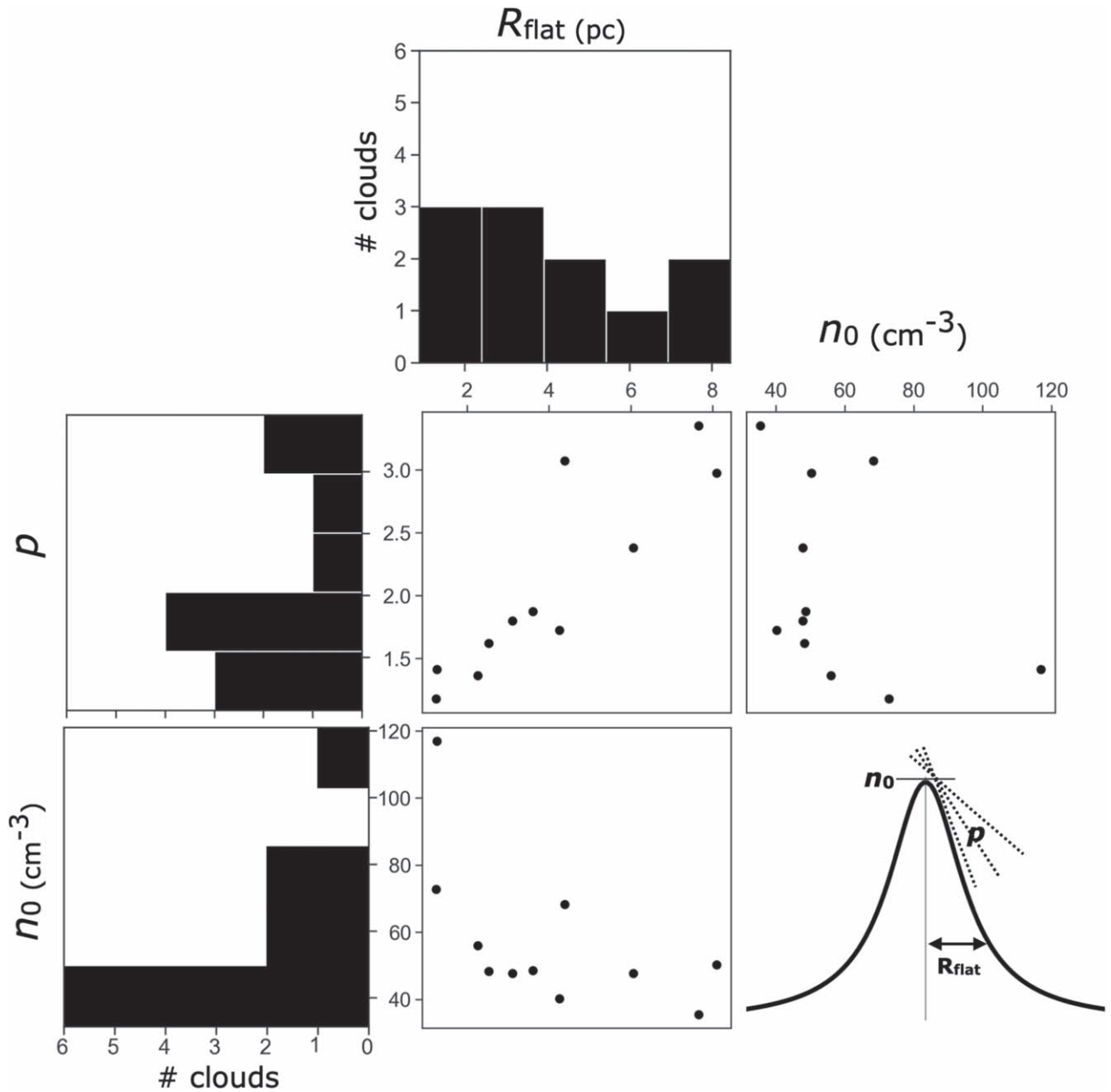
Figure 5. Summary of the radial volume density profile fitting results for the Plummer function, including the distribution of the flattening radius R_{flat}, the peak density n_0, and the index of the density profile p. Each point represents a single local cloud in the sample. We observe a strong degeneracy in the Plummer modeling, particularly between the R_{flat} and p parameters.

the inner 2 pc has a modest effect on our results, changing the widths on average by $\lesssim 20\%$ across all models. However, the quality of the fit degrades, validating our choice to remove the inner 2 pc of each radial profile in our main analysis.

4.3.5. Uncertainties in the Underlying 3D Dust Distribution

All results reported in this section are derived from the mean 3D dust distribution reported in Leike et al. (2020a). However, Leike et al. (2020a) also reported 12 different realizations of their dust distribution, which are used to derive the mean map. Because the different realizations reflect the underlying uncertainty in the 3D dust reconstruction, it is necessary to quantify the effect this uncertainty has on our results.

Accordingly, in Appendix E, we implement a more sophisticated fitting procedure, which simultaneously takes into account all 12 realizations of the 3D dust map when computing the model parameters. We find that overall, the uncertainty in the 3D dust map does not dominate our results, particularly for the two-component Gaussian fit, with best-fit parameters again typically changing $\lesssim 20\%$ across all clouds and all model fits. See Appendix E for full details.

4.3.6. Relationship between 3D Dust Correlation Kernel and Profile Shapes

Finally, to construct their 3D dust map, Leike et al. (2020a) modeled the dust as a log-normal Gaussian process, while
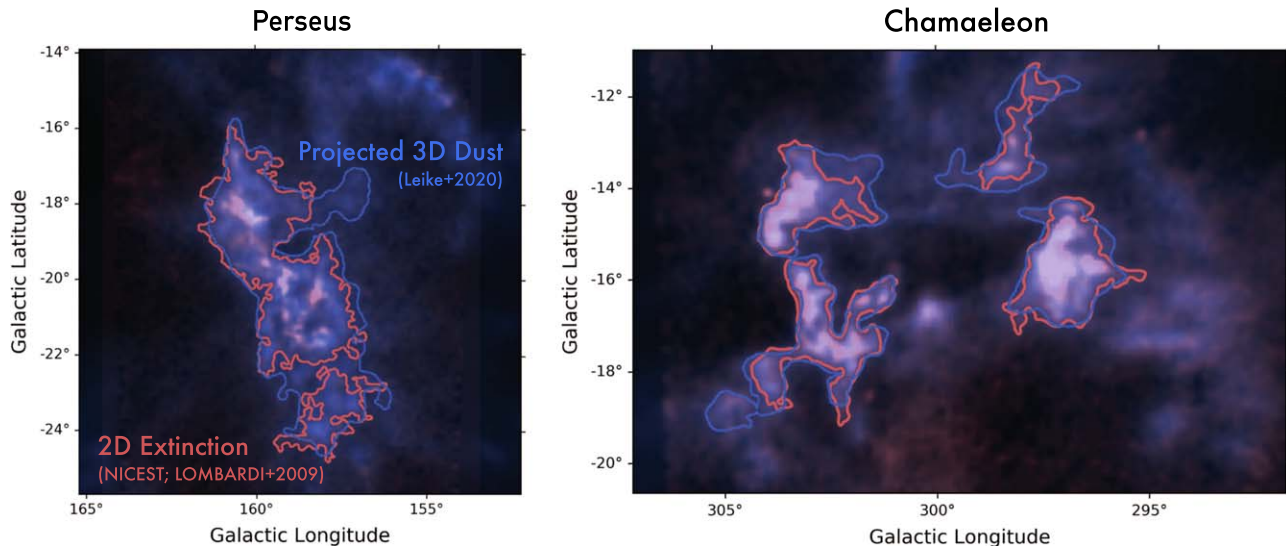
Figure 6. A comparison of the K-band extinction (A_K) maps derived from the NICEST algorithm (Lombardi 2009) (red) and from the Leike et al. (2020a) 3D dust map projected back on the plane of the sky (blue) for the Perseus Molecular Cloud (left panel) and Chamaeleon Molecular Cloud (right panel). The contours indicate the $A_K = 0.1$ mag cloud boundaries that are used to derive the clouds masses listed in Table 3.

simultaneously inferring the correlation kernel of the process, corresponding to the physical spatial correlation power spectrum of the dust. This correlation kernel acts as a prior on the dust extinction density.[20] The adoption of a log-normal Gaussian process prior was primarily chosen for statistical reasons, to ensure that the dust density is always positive, and to allow the dust density to vary by orders of magnitude. While this kernel is inferred from the data, it is necessary to quantify the similarity between the shapes of the radial profiles and the shape of the inferred kernel. If the shapes of the kernel and the profiles differ, it is likely that the data in the vicinity of the cloud directly determines the profile shapes. However, if the shapes of the kernel and profiles look similar, it is possible that the kernel is being imprinted on the clouds' structure.

In Appendix C and Figure C1 therein we compare the structure of our radial profiles to the structure of the Leike et al. (2020a) kernel inferred in the 3D dust map's reconstruction. We find that at radial distances between 0 and 10 pc, the cloud profiles deviate significantly from the kernel, indicating that their shapes are being driven by data local to the cloud. This deviation provides evidence that we are probing the *intrinsic* structure of the cloud at smaller radial distances. However, at large radii ($r > 10$ pc), the shapes of the kernel and the cloud profiles become increasingly similar, particularly for the Musca cloud. This similarity indicates that the cloud structure at lower densities may be driven by the prior on the dust extinction density. However, as the kernel is inferred using data inclusive of the cloud's structure (in addition to structure beyond each cloud of interest) the outer envelopes may still be physically meaningful. Accordingly, while we will discuss the physical significance of the profiles at lower densities in Section 6, we caution against over-interpretation of the tails of the radial volume density until the lower-density outer envelopes can be better validated in future work.

4.4. 2D Extinction Maps and Masses

In this section, we compare the cloud masses derived from 3D dust to those from traditional 2D dust approaches, with the goal of quantifying any discrepancies. In Figure 6, for the Perseus and Chamaeleon molecular clouds, we show a comparison between traditional 2D extinction maps (from the NICEST algorithm; Lombardi 2009, see Section 2.2) and 2D extinction maps derived by projecting 3D dust data (from Leike et al. 2020a, see Section 3.3) on the plane of the sky. Both maps have been convolved to the same (lower) angular resolution of the projected 3D dust maps, given the average distance to the cloud shown in Table 1. In the same figures, we overlay for both NICEST (red) and 3D dust (blue) the $A_K = 0.1$ mag contours used to derive cloud masses in Table 3. As will become more clear in Figure 7, despite being morphologically very similar at the $A_K = 0.1$ mag level, the NICEST maps are able to probe a much larger dynamic range of extinction in comparison to the Leike et al. (2020a) derived results. In particular, the NICEST maps show much more structure at the highest extinction levels, revealing clumps, cores, and filaments that are invisible in the Leike et al. (2020a) projected version.

This lack of structure at high extinction is not surprising, given how the Leike et al. (2020a) 3D dust map is produced. In order to probe highly extinguished regions (see Figure 6), any extinction-based dust-mapping method must be able to see stars *through* dust. In contrast to NICEST, which relies only on near-infrared photometry, the Leike et al. (2020a) analysis require Gaia optical photometry with relatively high signal-to-noise, which precludes stars behind dense regions from being included in the analysis. Another possible source of discrepancy between the Leike et al. (2020a) projected 3D dust and traditional 2D dust maps might stem from the calibration of the likelihood function used to construct the Leike et al. (2020a) 3D dust map. Specifically, the likelihood used in the construction of the Leike et al. (2020a) 3D dust map is calibrated using stars in lines of sight with approximately zero extinction, which could introduce biases in regions of higher extinction.

This missing high-extinction information in the Leike et al. (2020a) 3D dust map is more apparent in Figure 7, which compares

---

[20] The dust extinction density in the context of the Leike et al. (2020a) is the optical depth in the Gaia G-band per one parsec.

Table 3
Mass and Extinction Results

Cloud (1)	Mass$_{NICEST}$ (2) ($M_\odot$)	Mass$_{Leike}$ (3) ($M_\odot$)	$\frac{Mass_{NICEST}}{Mass_{Leike}}$ (4)	Maximum $A_{K,NICEST}$ (5) (mag)	Maximum $A_{K,Leike}$ (6) (mag)
Chamaeleon	4.9e+03	4.4e+03	1.1	1.19	0.29
Ophiuchus	9.4e+03	7.9e+03	1.2	1.99	0.31
Lupus	1.0e+04	8.9e+03	1.2	1.55	0.28
Taurus	1.6e+04	1.5e+04	1.0	0.90	0.38
Perseus	1.6e+04	1.3e+04	1.2	1.40	0.28
Musca	5.9e+02	4.9e+02	1.2	0.47	0.19
Pipe	8.5e+02	5.2e+02	1.6	1.29	0.23
Cepheus	1.2e+04	1.0e+04	1.2	1.15	0.33
Orion A[a]	3.2e+04	9.4e+03	3.4	1.48	0.34
Orion B[a]	2.9e+04	1.7e+04	1.7	1.34	0.33
λ Orionis[a]	1.2e+04	8.6e+02	13.7	1.36	0.22

Notes. Summary of mass and extinction results for local molecular clouds. (1) Cloud name. (2) Mass derived from a traditional 2D extinction map computed using the NICEST algorithm from Lombardi (2009). (3) Mass derived for the cloud from the Leike et al. (2020a) 3D dust map, which has been projected back on the plane of the sky. In both cases, the mass is computed above an $A_K = 0.1$ mag cloud boundary. (4) Ratio of the mass from columns (2) and (3). (5) Maximum A_K inside the cloud boundary based on the NICEST algorithm. (6) Maximum A_K inside the cloud boundary for the 2D extinction map derived from the 3D dust data. We provide a machine readable version of this table at the Harvard Dataverse (https://dataverse.harvard.edu/dataverse/cloud_topologies) (https://doi.org/10.7910/DVN/EIPHPR).
[a] Clouds below the horizontal line—Orion A, Orion B, and λ Orionis—should be treated with caution, as they lie at the very edge of the Leike et al. (2020a) 3D dust grid and are subjected to additional biases. Part of Orion A, toward the Orion Nebula Cluster, is also devoid of dust in the Leike et al. (2020a) 3D dust map despite being highly extinguished. See Section 5 for full details.

A_K PDFs for the inherently 2D NICEST technique (Lombardi 2009) and the 2D projection of the 3D maps (Leike et al. 2020a), across the full cloud sample. The histograms are computed by stacking every pixel above an $A_K = 0.1$ mag for every cloud. The A_K probability density function (PDF) for the Leike et al. (2020a) method shows more extinction than NICEST at low values ($A_K \approx 0.1$ mag), and much less (essentially no) extinction above an $A_K \approx 0.3$ mag. While the shapes of the two PDFs are ≈similar at the low extinction end ($A_K < 0.15$ mag), only the NICEST PDF shows a tail extending to high extinction ($A_K \approx 1.0$ mag). This high extinction tail manifesting in the NICEST maps is consistent with the maximum A_K we report on a cloud-by-cloud basis in Table 3. For the NICEST maps, the maximum A_K toward each cloud is ≈0.2–0.3 mag, while for NICEST it is a factor of a few higher, with peak $A_K = 0.9$–1.5 mag inside each cloud boundary. So, these comparisons suggest that the Leike et al. (2020a) map is a faithful representation of projected dust column density up to $A_K = 0.2$–0.3 mag, equivalent to $A_V = 2$–3 mag.

How does reduced sensitivity at high extinction affect masses derived from the Leike et al. (2020a) map? Table 3 lists masses for clouds (above their $A_K = 0.1$ mag boundaries; see Section 3.4) computed using both methods and the *ratio* of those masses. In general, the ratio is near unity because mass at high extinction makes up a small fraction of clouds' total mass (see also e.g., Lada et al. 2010). In all cases, NICEST masses are larger, but not by a significant amount: the ratio of the NICEST mass to the 3D dust mass ranges from 1.0 to 1.6, with an average of 1.2, for the "complete clouds," listed above the line in Table 3. Discrepancies, as should be expected, are significant for the "incomplete" clouds (below the line, Orion A, Orion B, and λ Orionis) which lie at the edge of the Leike et al. (2020a) 3D dust map. While the mass ratio for Orion B is only modestly higher than the rest of the sample ($\frac{Mass_{NICEST}}{Mass_{Leike}} = 1.7$), the NICEST mass for Orion A is 3.4× larger than its 3D dust derived mass, and for λ Orionis it is 13.7× as large. This high ratio indicates that while Orion B is largely

complete, significant amounts of mass are missing for Orion A and λ Orionis, not only because the Leike et al. (2020a) method is not sensitive enough at high extinction, but also likely because some fraction of the mass lies beyond the Leike et al. (2020a) grid.

5. Cloud-by-cloud Exposition

In this section, we summarize the skeletonization and radial profile fitting results of Section 4 on a cloud-by-cloud basis, and in light of complementary results for each cloud from the literature. A gallery of 3D interactive figures for the full sample is available here.[21]

5.1. Chamaeleon

As shown in Figure 2 (interactive), we find that the skeleton of the Chamaeleon Molecular Cloud is located at distances between 173 and 190 pc, with a median distance of 183 pc. Curiously, and as apparent in Figure 2, we find that all the Chamaeleon clouds—Chamaeleon I, II, and III—are connected via a hub-like structure, with a void in the center. The Chamaeleon complex is also physically connected to the Musca dark cloud at a distance of 172 pc. Musca is also shown in the 3D dust map in Figure 2 but skeletonized separately in this work.

Based on two-component Gaussian fitting results, Chamaeleon has an inner envelope full-width at half maximum (FWHM = 2.35σ) of 6.8 pc, and an outer envelope FWHM of 24 pc, with a ratio of the outer to inner width equal to 3.5.

5.2. Ophiuchus

As shown online[22] (interactive), we find that the skeleton of Ophiuchus is located at distances between 115 and 150 pc. The

[21] https://faun.rc.fas.harvard.edu/czucker/Paper_Figures/3D_Cloud_Topologies/gallery.html
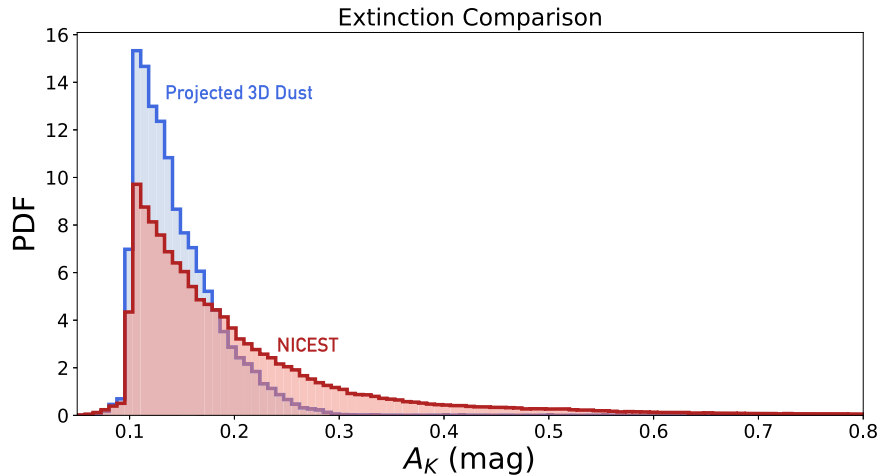[22] https://faun.rc.fas.harvard.edu/czucker/Paper_Figures/3D_Cloud_Topologies/ophiuchus_topology/ophiuchus.html

Figure 7. Comparison of the probability density functions (PDFs) between the K-band extinction (A_K) derived from the 2D NICEST algorithm (Lombardi 2009) (red) and from the Leike et al. (2020a) 3D dust map projected back on the plane of the sky (blue). We only consider structure above the $A_K = 0.1$ mag threshold used to derive the cloud masses in Table 3. We extract the extinction distribution above this $A_K = 0.1$ mag boundary for each cloud, and then stack the per-cloud results to obtain a representative histogram for each method. The histograms are normalized such that their total area is equal to one. While similar at the $A_K \approx 0.1$ mag level, traditional 2D dust extinction maps show a larger dynamic range, with increased sensitivity at higher extinction ($A_K \gtrsim 0.2$–0.3 mag).

median distance is 136 pc (also the distance of L1688), which is consistent with previous distance estimates based on 3D dust mapping (from Zucker et al. 2019, 2020) and from very long baseline interferometry (VLBI) parallax measurements of YSOs (from Ortiz-León et al. 2017). There is a 10 pc distance gradient across the B44 streamer, which extends from ρ Ophiuchus out to a distance of $d \approx 145$ pc. The farthest component is the "arc" of Ophiuchus, lying at $d \approx 150$ pc, while the nearest component is the Ophiuchus north complex, lying between $d \approx 115$ and 125 pc. The effect of feedback from OB stars (e.g., σ Sco, δ Sco) on the 3D distribution of dust, in particular the formation of the elongated streamers B44 and B45, will be discussed in detail in J. Alves et al. (2021, in preparation). While B44 appears as part of the main spine of Ophiuchus, B45 appears as a skeletal branch that is pruned prior to the width analysis. We find that the B45 streamer extends from B44, rather than from the core L1688 region. We believe that, with a typical width of $\approx$1 pc, this is an artifact of B45 being only marginally resolved in the Leike et al. (2020a) 3D dust, rather than a reflection of the true morphology of the B45 streamer.

Based on the two-component Gaussian fitting results, Ophiuchus has an inner envelope FWHM of 6.3 pc, and an outer envelope FWHM of 24 pc, with a ratio of the outer to inner width equal to 3.8.

5.3. Lupus

As shown online[23] (interactive), the skeleton of the Lupus molecular cloud lies between 155 and 198 pc, with a median distance of 165 pc. On a region-by-region basis, we find Lupus 9 to be the farthest cloud in the complex, at a distance of $\approx$197 pc. Lupus 3–8 are all connected within the same complex in 3D space (at the level of our thresholding algorithm, $n = 35$ cm^{-3}) at a distance of $\approx$163 pc. Lupus 1 lies the closest in distance, at $\approx$155 pc, though the Lupus 1 line of sight suffers from confusion. By confusion, we mean that there is evidence of multiple components along the line of sight, in that there is a

component immediately to the south of Lupus 1 (appearing to connect to Lupus 1 on the plane of the sky) but which lies at a much farther distance of 190 pc. Our distances to Lupus 1, 3, 4, 5, and 6 are broadly consistent with those from Galli et al. (2020b), whose distances range from 150 to 160 pc based on Gaia DR2 astrometry toward young stars associated with the complex. Curiously, we find no prominent feature at higher gas densities ($n > 35$ cm^{-3}) associated with Lupus 2. However, Galli et al. (2020b) placed Lupus 2 at a distance of 158 pc, suggesting that it is indeed associated with the Lupus 1, 3, 4, 5, and 6 regions.

Based on the two-component Gaussian fitting results, Lupus has an inner envelope FWHM of 6.1 pc, and an outer envelope FWHM of 19 pc, with a ratio of the outer to inner width equal to 3.1.

5.4. Taurus

As shown online[24] (interactive), the skeleton of the Taurus Molecular Cloud extends between 131 and 168 pc. When viewed from the top down, it is evident that Taurus is comprised of dust in two different layers, separated on average by about 10–15 pc. This layering is consistent with several previous studies, which have found evidence of significant depth effects (see, e.g., Galli et al. 2018, 2019; Zucker et al. 2019) over this same distance range. The furthest component of Taurus, at a distance of 168 pc, is an elongated component of the cloud extending out from L1538 toward $(l, b) = (177°.5, -8°.5)$.

Based on the two-component Gaussian fitting results, Taurus has an inner envelope FWHM of 6.1 pc, and an outer envelope FWHM of 28 pc, with a ratio of the outer to inner width equal to 4.6.

5.5. Perseus

As shown in Figure 1 (interactive), the skeleton of the Perseus Molecular Cloud extends between 279 and 301 pc. It exhibits a prominent $\approx$20 pc distance gradient. This distance

---

[23] https://faun.rc.fas.harvard.edu/czucker/Paper_Figures/3D_Cloud_Topologies/lupus_topology/lupus.html

[24] https://faun.rc.fas.harvard.edu/czucker/Paper_Figures/3D_Cloud_Topologies/taurus_topology/taurus.html

gradient is very similar to that found independently in Zucker et al. (2018b), which also used 3D dust mapping to obtain distances to star-forming regions across Perseus, finding them to be located between 279 and 302 pc. This gradient is also broadly consistent with the VLBI parallax results toward young stars in Perseus from Ortiz-León et al. (2018), though Ortiz-León et al. (2018) found IC 348 to be at a distance of 320 pc, about 20 pc farther away than we find either in this work or in Zucker et al. (2018b). Upon further examination of the distribution of the 3D dust and young stars in this region, we find that neither the Zucker et al. (2018b) nor Ortiz-León et al. (2018) distance to IC 348 is inaccurate. Rather, it appears that the IC 348 stellar cluster has actually migrated beyond the distance of the dust cloud from which it formed, which results in the discrepancy between the dust- and star-based approaches. This migration is consistent with the estimated age of IC 348 of $\approx 2-6$ Myr (Muench et al. 2007). No such discrepancy is found for the younger NGC1333 cluster. When considering solely the 3D dust distribution, neglecting information from YSOs, no component of Perseus lies beyond 300 pc.

Based on the two-component Gaussian fitting results, Perseus has an inner envelope FWHM of 9.6 pc and an outer envelope FWHM of 28 pc, with a ratio of the outer to inner width equal to 2.9.

5.6. Musca

As shown online[25] (interactive), the Musca dark cloud is located between distance of 171 and 173 pc. We find no evidence that Musca is a sheet viewed edge-on, but rather is a true filament in 3D space (see Tritsis & Tassis 2018). It is physically connected to the Chamaeleon Molecular Cloud complex at a level of $n = 35 \, \mathrm{cm}^{-3}$ but is skeletonized separately in this work to obtain an independent width.

Based on the two-component Gaussian fitting results, Musca has an inner envelope FWHM of 7.3 pc, and an outer envelope FWHM of 42 pc, with a ratio of the outer to inner width equal to 5.8. Musca is a clear outlier in the distribution of its outer Gaussian profile, which is significantly larger and more extended than the rest of the sample. At large radial distances, the shape of Musca's radial profile shows the highest correspondence to that of the underlying kernel inferred during the reconstruction of the Leike et al. (2020a) 3D dust map (see Section 4.3.6 and Appendix C), indicating that this highly extended envelope is likely prior-dominated. In addition to the outer envelope being prior-dominated, we also believe that the inner envelope of Musca—manifesting as an infrared dark cloud—is unresolved in our map, as 2D dust results targeting the infrared dark component of the cloud find widths as small as a few tenths of a parsec (Cox et al. 2016). As a result, we urge extreme caution when interpreting these width results.

5.7. Pipe

As shown online[26] (interactive), the Pipe dark cloud is located between a distance of 147 and 163 pc, with a 15 pc distance gradient. The stem of the Pipe nebula, near B59, is located at a distance of 150 pc, and the bowl, extending down to latitudes of $b = 2°.4$, lies as far as 163 pc. About halfway down the stem, a thin tendril of gas connects the Pipe nebula with the Ophiuchus cloud complex, meeting an extension of Ophiuchus

that reaches beyond the B44 streamer. However, the Pipe nebula is skeletonized separately from Ophiuchus in this work, in order to obtain an independent width. The distance to B59 in the stem of the Pipe nebula is smaller than, but still consistent with, independent Gaia parallax measurements of YSOs in the complex (163 pc, from Dzib et al. 2018).

Based on the two-component Gaussian fitting results, the Pipe nebula has an inner envelope FWHM of 9.6 pc and an outer envelope FWHM of 23 pc, with a ratio of the outer to inner width equal to 2.4. This ratio of the outer to inner width is the smallest of all clouds in the sample.

5.8. Cepheus

As shown online[27] (interactive), the skeleton of the Cepheus molecular cloud is located between distances of 337 and 370 pc, with a median distance of 345 pc. Our skeletonization only includes the northern section of Cepheus, as the southern section (closer to the Galactic plane) actually lies at distances >900 pc (Grenier et al. 1989; Zucker et al. 2019). The median skeleton distance is in excellent agreement with the average Cepheus "near" distance of 352 pc, based on an independent 3D dust-mapping pipeline from Zucker et al. (2019). Our Cepheus skeletonization includes four isolated density features at a level above our chosen threshold ($n = 35 \, \mathrm{cm}^{-3}$), the highest of any cloud in the sample. These features include the sub-regions L1148/L1552/L1155 ($d = 338$ pc), L1172 ($d = 340$ pc), L1228 ($d = 368$ pc), L1241 ($d = 349$ pc), and L1247/L1251 ($d = 340$ pc).

Based on the two-component Gaussian fitting results, Cepheus has an inner envelope FWHM of 5.9 pc, and an outer envelope FWHM of 26 pc, with a ratio of the outer to inner width equal to 4.4.

5.9. Corona Australis

As shown online[28] (interactive), the skeleton of the Corona Australis cloud is located between distances of 136 and 179 pc, with a median distance of 161 pc. Corona Australis is one of the fluffiest local clouds in the Leike et al. (2020a) map and has no significant extended features above a density threshold of $n = 35 \, \mathrm{cm}^{-3}$ so it is skeletonized at a much lower level ($n = 5 \, \mathrm{cm}^{-3}$) to provide distance information. We find that the Corona Australis cloud exhibits a prominent distance gradient, with the head of the cloud about 20–30 pc closer than the tail. The most extinguished part of Corona Australis, which manifests as a dark cloud at optical wavelengths, lies at a distance of $d = 144$ pc, which is in good agreement with the results of Galli et al. (2020a; 149 pc), and Zucker et al. (2019; 151 pc). The reason that we determine a higher overall median spine distance is due to the existence of Corona Australis' diffuse tail, which extends as far as 179 pc at a latitude of $b = -26°$.

5.10. Orion A

As shown online[29] (interactive), we determine that the skeleton of the Orion A cloud spans distances of 391–445 pc,

---

[25] https://faun.rc.fas.harvard.edu/czucker/Paper_Figures/3D_Cloud_Topologies/musca_topology/musca.html

[26] https://faun.rc.fas.harvard.edu/czucker/Paper_Figures/3D_Cloud_Topologies/pipe_topology/pipe.html

[27] https://faun.rc.fas.harvard.edu/czucker/Paper_Figures/3D_Cloud_Topologies/cepheus_topology/cepheus.html

[28] https://faun.rc.fas.harvard.edu/czucker/Paper_Figures/3D_Cloud_Topologies/coraus_topology/coraus.html

[29] https://faun.rc.fas.harvard.edu/czucker/Paper_Figures/3D_Cloud_Topologies/oriona_topology/oriona.html

with a median distance of 405 pc. The 3D dust distribution toward Orion A is peculiar, due to the fact that there is a large piece of the cloud missing toward the Orion Nebula Cluster— the densest part of the entire complex. This lack of dust is *not physical*, and represents the inability of the Leike et al. (2020a) to fully probe high gas densities. As a result, the head (toward the Orion Nebula Cluster) and tail of Orion A (toward L1647) appear not to connect as they should in 3D space. Analysis of Orion's YSO distribution (Großschedl et al. 2018) and other high resolution 3D dust maps of Orion A (Rezaei Kh. et al. 2020) clearly show that the head and tail *are* physically connected. The missing ONC region could explain in part the significant discrepancy between the cloud mass derived from 2D dust extinction versus from the projected 3D dust distribution (see Section 4.4).

In general, we find good agreement with previous studies toward regions probed by the dust map, as well as a similar *range* of distances. For example, Großschedl et al. (2018) found that the bulk of the Orion A cloud lies between distances of $d \approx 380\text{--}460$ pc, which is not inconsistent with our spread of 391–445 pc. However, there is no visible connection between the farthest point in Orion A (L1647-S at a distance of 445 pc) and the main Orion A cloud consisting of L1641, while this connection *does* appear in other approaches (Großschedl et al. 2018; Rezaei Kh. et al. 2020). This lack of connection at the tail could be physical, or it could be indicative of another missing mass situation, like toward the Orion Nebula Cluster. In addition to mass missing *within* the grid, it is also possible that there is mass missing *beyond* the grid, as Orion A lies at the boundary of the Leike et al. (2020a) dust mass. Thus, our skeletonization and width analysis results for Orion A should be treated with more caution than for other "complete" clouds. The most likely effect of Orion A lying at the edge of the grid is that we will slightly underestimate the distance to the complex.

Based on the two-component Gaussian fitting results, we find that Orion A has an inner envelope FWHM of 6.8 pc and an outer envelope FWHM of 20 pc, with a ratio of the outer to inner width equal to 2.9.

5.11. Orion B

As shown online[30] (interactive), we determine that the skeleton of the Orion B cloud spans distances of 397–406 pc, with a median distance of 404 pc. Our median distance is consistent with Kounkel et al. (2018), which leverages Gaia Data Release 2 (DR2) parallax measurements toward young stars in the complex to obtain a distance of 407 ± 4 pc. Unlike Orion A, we find no evidence of a strong distance gradient, and also find that Orion B consists of a single density feature with a length of 69 pc. However, because Orion B again lies at the very edge of the Leike et al. (2020a) dust map, it is possible that parts of Orion B could still be missing, which would bias our distance estimates lower compared to a cloud that lies well within the map boundaries. Thus, like our skeletonization and width analysis results for Orion A, we caution that our results for Orion B should be treated with more caution than for other "complete" clouds.

Based on the two-component Gaussian fitting results, Orion B has an inner envelope FWHM equal of 11.4 pc and an outer

envelope FWHM of 34 pc, with a ratio of the outer to inner width equal to 3.0.

5.12. λ Orionis

Finally, as shown online[31] (interactive), we determine that the skeleton of the λ Orionis cloud spans distances of 375–397 pc, with a median distance of 386 pc. A clear ring-like morphology is observed in 2D dust extinction maps, which Dolan & Mathieu (2002) argued formed from ejected material driven by a supernovae blast at the center of the ring about 1 Myr ago.

We observe the same ring-like morphology in 3D. However, the skeletonization, and resulting widths, should be considered with extreme caution, as the skeleton lies only a few parsecs from the boundary of the Leike et al. (2020a) 3D dust map, so the skeletonization is likely to underestimate the cloud's distance. There is clearly mass missing in the λ Orionis region, given that the mass for the cloud based on 2D dust maps (from NICEST) is a factor of 14 higher than what we calculate using just the 3D dust volume local to the cloud (see Section 4.4 and Table 3). Consistent with this missing mass scenario, average distances to the λ Orionis region tend to be higher in other studies (e.g., 402 pc from Zucker et al. 2020). The average distance to λ Orionis from Zucker et al. (2020) is also consistent with independent distances of young stars, for which Kounkel et al. (2018) obtained $d = 404$ pc.

Based on the two-component Gaussian fitting results, λ Orionis has an inner envelope FWHM of 8.7 pc and an outer envelope FWHM equal of 30 pc, with a ratio of the outer to inner width equal to 3.4. Despite only measuring the cloud width using voxels in front of λ Orionis (due to the Leike et al. 2020a grid ending directly beyond the spine), these results are consistent with results for the "complete" clouds.

6. Discussion

In Section 4, we have shown that the radial volume density profiles measured in 3D for local molecular clouds are well-described by two functions: a two-component Gaussian function and a Plummer function. A single-component Gaussian is universally a poor fit to the data. We have also shown that the Leike et al. (2020a) technique is capturing a majority of the cloud mass for all "complete" clouds in the sample, deviating from 2D integrated dust extinction measurements (from the NICEST methodology; Lombardi 2009; Lombardi et al. 2011) only at higher extinction ($A_K \gtrsim 0.3$ mag). In this section, we discuss the potential implications of our results, and provide an initial comparison of the 2D and 3D shapes of the radial profiles for a subset of the sample, as a basis for future work.

6.1. Two-component Gaussian—Probing a Phase Transition?

In terms of the two-component Gaussian model, one possible explanation for the shape of the radial density profiles is that we are probing gas in different phases, where the transition between the outer and inner Gaussian profiles represents a shift in temperature, density, and/or chemical composition of the gas. In the density range consistent with our radial profiles, possible transitions include a chemical transition between atomic and molecular hydrogen (the H I-to-H_2 transition), or a

---

thermal transition between the unstable neutral medium (UNM) and cold neutral medium (CNM), driven by the temperature dependence of the atomic cooling curve. While the data are suggestive, we do not yet have enough detailed evidence to prove the link between the shape of the radial volume density profiles and a phase transition. Thus, in what follows, we only seek to present a plausibility argument.

6.1.1. Chemical Transition between Atomic and Molecular Gas

The first explanation for the bimodality in the radial profiles is that the broader, lower amplitude "outer" Gaussian probes the shape of the atomic H I gas envelope, while the narrower higher amplitude "inner" Gaussian probes the molecular phase. If so, the noticeable break in volume density coincident with the start of the inner Gaussian would represent a chemical transition of the gas, delineating the radial distance in 3D space, at which point molecular hydrogen becomes self-shielded. Models suggest that the transition to self-shielding—at which point molecular hydrogen can persist—can be either sharp or gradual, depending on the strength of the ultraviolet (UV) radiation field relative to the gas density. However, once a critical column density of H_2 has been produced, the fraction of hydrogen in molecular form should rise rapidly (Krumholz et al. 2008; Sternberg et al. 2014; Bialy & Sternberg 2016). If this transition is occurring in local molecular clouds—as predicted by analytic theory—it might explain why we find the two-component Gaussian model to be so strongly favored over a single-component Gaussian model.

We have known for a few decades that H I envelopes around molecular clouds are common (see, e.g., Williams et al. 1995; Williams & Maddalena 1996; Moriarty-Schieven & Wannier 1997). These H I envelopes are significantly extended with respect to the molecular gas and may be either the remnants of atomic clouds that condensed to form GMCs, or photodissociated gas on the outskirts of the molecular cloud. More likely, the atomic envelope arises from a combination of both phenomena. In addition to being observed in solar neighborhood clouds (e.g., in Perseus and Taurus; see Stanimirovic et al. 2014; Lee et al. 2015; Pascucci et al. 2015) and toward the inner galaxy (Bialy et al. 2017; Beuther et al. 2020), atomic envelopes have also been observed at much lower resolution in the nearby Large Magellanic Cloud (Fukui et al. 2009). Recent numerical simulations characterizing the properties of highly resolved synthetic molecular clouds (e.g., Duarte-Cabral & Dobbs 2016; Seifried et al. 2017) also note the presence of large extended H I envelopes.

We find that the typical amplitudes of the outer Gaussian profiles are consistent with the typical densities of the atomic envelopes seen in observations, mainly via H I emission on the plane of the sky. In this study, the peak densities of the outer envelopes—characterized by the amplitude parameter a_2—span $n = 5$–$15\,cm^{-3}$, with an average amplitude of $n = 9\,cm^{-3}$, falling off to only a few particles per cubic centimeter at large radii. This range is consistent with H I densities inferred for atomic envelopes around molecular clouds in both observations and simulations. Looking at a sample of 123 H I envelopes in the Large Magellanic Cloud, Fukui et al. (2009) derived a typical envelope density of $10\,cm^{-3}$, calculated by dividing each cloud's H I column density by its approximate size on the plane of the sky.[32] Using Galactic Arecibo L-band Feed Array (GALFA) H I and Infrared

Astronomical Satellite (IRAS) data, Bialy et al. (2015) also calculated the atomic hydrogen volume density toward the Perseus molecular cloud, finding that the atomic densities vary between $n = 2$ and $11\,cm^{-3}$. This range of densities is similar to the range of densities captured by the outer Gaussian in the radial volume density profile that we measure for Perseus, spanning $n = 12\,cm^{-3}$ toward the spine, down to $n \approx 2\,cm^{-3}$ toward the outskirts of the cloud.

In terms of the inner Gaussian, we find typical peak densities —parameterized by a_1—to lie between $n \approx 25$ and $52\,cm^{-3}$. While the amplitude for the averaged profile is of this order, a significant fraction of cuts show peak densities with $n = 100\,cm^{-3}$, with some extending as high as $n = 200\,cm^{-3}$. While these average volume densities are not high enough to be observationally probed by CO-bright molecular gas manifesting at $n \gtrsim 200\,cm^{-3}$ (see e.g., Busch et al. 2019), they are consistent with densities of so-called "CO-dark" gas, a phase associated with warmer, more diffuse molecular hydrogen that is not detectable in CO or H I. While invisible in both CO and H I, γ-ray observations—capable of tracing a cloud's gas mass independent of its chemical state—show that diffuse molecular gas surrounds all nearby CO-detected molecular clouds targeted in this study. This CO-dark phase effectively acts as an observational bridge between clouds' extended atomic envelopes and their embedded CO-bright cores (Grenier et al. 2005), and would mark the true chemical transition between atomic and molecular gas. Tang et al. (2016) used [C II] emission to trace CO-dark diffuse molecular gas in the Galactic plane, finding that this gas manifests at a range of densities (from $n \approx 60$–$1000\,cm^{-3}$), with an average density of $n \approx 200\,cm^{-3}$.[33] The average density from Tang et al. (2016) is a factor of a few larger than our average peak density a_1, but the lower estimates from Tang et al. (2016) remain consistent with our results. Also consistent with these observations, analysis of the CO-dark diffuse molecular gas for synthetic clouds from the SILCC-Zoom project (Seifried et al. 2019) find number densities between 10 and $1000\,cm^{-3}$, with an average density of CO-dark gas on the order of $100\,cm^{-3}$—only a factor of two higher than what we estimate here for the inner Gaussian. Given that the volume densities derived from the 3D dust data —particularly for the inner Gaussian component—should be lower limits (see also Section 2.1.2), our results are generally in agreement with literature estimates for CO-dark molecular gas from both observations and simulations.

Finally, there is a straightforward test to disprove this H I-to-H_2 transition hypothesis, involving a comparison between the radial extent of CO emission projected on the plane of the sky and radial extent of the inner Gaussian component derived here. The detection of CO emission significantly beyond the boundaries of the inner Gaussian profile would be in direct contradiction to the proposed origin, because no molecular gas should lie beyond the inner Gaussian. To test this scenario, we build CO radial profiles for a subset of the clouds in the sample, as described in detailed in Appendix F. We find that the CO profiles shows widths equal to or marginally smaller than that of the inner Gaussian profiles, which is consistent with the scenario that the inner Gaussian profiles could be tracing CO-dark gas.

---

[32] We note, however, that the H I-to-H2 transition strongly depends on the dust-to-gas ratio, and the Large Magellanic Cloud has lower metallicity than Milky Way (Van der Swaelmen et al. 2013), so any direct comparison between the two systems should be treated with caution.

[33] While [C II] emission is commonly used as a tracer of CO-dark gas, we note that a recent study by Hall et al. (2020) toward the local Perseus Molecular Cloud concludes that a [C II] envelope can also arise from the CNM phase, without a need to invoke CO-dark molecular gas.

6.1.2. Thermal Transition between Unstable and Cold Neutral Medium

While a diffuse molecular gas component offers one explanation for the shape of the inner Gaussian profile, no H_2 component necessarily needs to be invoked to explain the clouds' density structure. It is well established that the atomic neutral medium consists of two thermally stable states at significantly different densities and temperatures—the warm neutral medium (WNM) at $n \approx 0.2$–$0.9 \, \mathrm{cm}^{-3}$ and the CNM at $n \approx 7$–$70 \, \mathrm{cm}^{-3}$ (Field et al. 1969; Wolfire et al. 2003; Murray et al. 2018b). This two-phase structure is a natural consequence of the density and temperature dependence of the cooling curve at play in the diffuse interstellar medium. While the peak densities we find for the inner Gaussian ($a_1 = 25$–$52 \, \mathrm{cm}^{-3}$) are consistent with lower-density estimates of CO-dark diffuse molecular gas, they are also in strong agreement with the densities of the CNM. However, the peak densities of the outer envelopes are much larger than expected for the WNM. In traditional two-phase models, H I at intermediate temperatures should be expected to quickly evolve into one of the stable phases. However, ample evidence has recently suggested that a significant fraction of Galactic H I lies in the thermally unstable phase, driven by dynamical processes in the interstellar medium (e.g., turbulence; see Heiles & Troland 2003; Roy et al. 2013; Murray et al. 2018b). Thus, if the inner envelope is probing the CNM, then the outer envelopes (with peak densities $a_2 = 5$–$15 \, \mathrm{cm}^{-3}$) may probe the thermally unstable H I lying at densities between the WNM and CNM with $n \approx 1$–$10 \, \mathrm{cm}^{-3}$. The transition observed in the two-component Gaussian profiles would then be driven not by a change in the chemical state of the gas, but by a change in the thermal phase of the atomic neutral medium.

Consistent with this scenario, Murray et al. (2018b) analyzed H I spectra toward 57 lines of sight taken from the 21-SPONGE survey to infer the fraction of H I mass in the thermally unstable regime, finding that 20% is in the UNM phase, as opposed to 28% in the CNM phase (with the remaining mass in the WNM phase). Murray et al. (2018b) further found no significant difference in the UNM fraction as a function of latitude, with both high- ($|b| > 10°$) and low-latitude lines of sight showing similar mass distributions. Given its ubiquity, both from Murray et al. (2018a) and complementary studies (Heiles & Troland 2003; Roy et al. 2013), the UNM-to-CNM transition represents a viable alternative to the H I-to-H_2 transition for explaining the two-component Gaussian shape of the radial profiles. We note, however, that while the Murray et al. (2018b) lines of sight span a wide range in latitudes, none of them intersect the clouds targeted in this work.

Nevertheless, to broadly verify the consistency of our results with those of Murray et al. (2018b), we can compare for each cloud the relative amount of mass contained in the outer and inner envelope. If our results are consistent with Murray et al. (2018b), we would expect the ratio of the outer and inner envelope masses to be $\frac{M_2}{M_1} = \frac{M_{\mathrm{UNM}}}{M_{\mathrm{CNM}}} = \frac{20\%_{\mathrm{UNM}}}{28\%_{\mathrm{CNM}}} = 0.71$. We compute this ratio in two ways. First, we compute the mass of the inner envelope, M_1, and outer envelope M_2 by taking the definite integral of the Gaussian density profiles (shown via the black–white dotted and cyan–black dotted curves in, e.g., Figure 1) over the volume, assuming a cylindrical geometry

$$M_1 = 2\pi l \, \mu m_p \int_{-\infty}^{+\infty} a_1 e^{\frac{-r^2}{2\sigma_1^2}} \, r \, dr$$

$$M_2 = 2\pi l \, \mu m_p \int_{-\infty}^{+\infty} a_2 e^{\frac{-r^2}{2\sigma_2^2}} \, r \, dr$$

where the parameters a_1, σ_1, a_2, σ_2 are the same as those reported in Table 2, $\mu = 1.37$ is the mean molecular weight, corrected for the helium abundance, m_p is the mass of a proton, and l is the length of the cloud reported in Table 1. Computing M_1 and M_2 numerically and taking the ratio across the sample we obtain a median ratio for $\frac{M_2}{M_1} = 2.9$, with a spread of 1.3, which is higher than the predicted Murray et al. (2018b) results of 0.72. Given that we are likely underestimating the densities in potentially CNM-associated regions, one possible explanation is that while the typical extents of the inner and outer components could be correct, their amplitudes, particularly for the inner Gaussian, may not be. Thus, a second, more extreme way to test this is to assume that the inner envelope is entirely composed of CNM, and UNM only exists beyond the edge of the inner envelope. To compute this, we create cylindrical representations of the inner and outer envelopes, where the width of each 3D cylinder is equivalent to the FWHM derived from the σ_1 and σ_2 values reported in Table 2 (FWHM = $2.355 \times \sigma$). These cylinders are toggleable on and off in the gallery of interactive cloud figures.[34] The cylinders define a mask in 3D volume density space over which the masses are computed:

$$M_{\mathrm{cylinder_{inner}}} = \Sigma_i \, \mu m_p \times n_{i,\mathrm{inner}} \, dV$$

$$M_{\mathrm{cylinder_{outer}}} = \Sigma_i \, \mu m_p \times n_{i,\mathrm{outer}} \, dV.$$

Here, dV is the volume element of an individual voxel i in the 3D volume density map, equal to 1 pc^3. The $\Sigma_i \, n_{i,\mathrm{inner}}$ and $\Sigma_i \, n_{i,\mathrm{outer}}$ terms represent the sum over the set of voxels (in gas density space n), which lie within the 3D inner and outer cylindrical regions, respectively. Under the assumption that no UNM lies within the bounds of the inner envelope, the resulting mass ratio would be

$$\frac{M_2}{M_1} = \frac{M_{\mathrm{cylinder_{outer}}} - M_{\mathrm{cylinder_{inner}}}}{M_{\mathrm{cylinder_{inner}}}}.$$

As expected, we calculate a lower value of $\frac{M_2}{M_1}$, with a median of 2.1 and a spread of 1.0. In reality the true mass ratio is likely somewhere between the two examples given here, and additional follow-up work will be needed to rule out the possibility of a UNM-to-CNM transition.

6.1.3. Constant Ratio between Outer and Inner Cloud Envelopes

Regardless of whether the transition between the outer and inner envelopes is due to a (a) chemical transition between H I and H_2 gas (b) a thermal transition between the UNM and the CNM; or neither, we find that the ratio between the widths of the outer and inner envelopes across the sample is roughly 3.4, with a relatively small scatter of ≈ 1. This ratio could be physically significant, with the potential to constrain the formation timescale of H_2, or the rate at which gas flows between different thermal phases of the diffuse interstellar medium (e.g., between the UNM and CNM). More targeted analytic modeling (e.g., in the style of Krumholz et al. 2009;

---

[34] https://faun.rc.fas.harvard.edu/czucker/Paper_Figures/3D_Cloud_Topologies/gallery.html

Sternberg et al. 2014; Bialy & Sternberg 2016), further contextualization with CO and H I spectral-line maps, and comparisons to simulations that track H I, H₂, and CO formation and destruction in a time-dependent chemical network (e.g., the Cloud Factory Simulations; Smith et al. 2020) should shed more light on this behavior.

6.2. An Isothermal Self-gravitating Cylinder?

For the past 10 years, Plummer models (originally describing the stellar surface density of globular clusters; Plummer 1911) have often been used to characterize the radial profiles of filaments extracted from H_2 column density maps as part of the Herschel Gould Belt Survey (André et al. 2010). These studies (Arzoumanian et al. 2011, 2019; Palmeirim et al. 2013; Cox et al. 2016) adopt an idealized Plummer-like analytic model for the (column) density profile of a cylindrical filament, featuring a denser, flat inner portion and an outer portion that falls off like a power law at larger radii:

$$n(r) = \frac{n_0}{[1 + (r/R_{\text{flat}})^2]^{p/2}} \longrightarrow \Sigma(r)$$
$$= A_p \frac{N_0}{[1 + (r/R_{\text{flat}})^2]^{\frac{p-1}{2}}}, \qquad (9)$$

where $n(r)$ describes the volume density profile adopted throughout this work, and $\Sigma(r)$ is the corresponding column density profile employed in the literature, with N_0 the peak column density, R_{flat} the flattening radius, p the index of the density profile, and A_p is a constant factor that accounts for the filament's inclination angle to the plane of the sky. In column density studies, the inclination of the filament to the plane of the sky is assumed to be zero, which is not the case in our volume density analysis. Following the formalism outlined in Ostriker (1964) and Equation (9), the density structure of an isothermal, self-gravitating gaseous cylinder in hydrostatic equilibrium corresponds to a special case with a power-law index $p = 4$ or $n \propto r^{-4}$ at large radii ($r \gg R_{\text{flat}}$). Analyzing the Herschel column density distribution of filaments, various works (Arzoumanian et al. 2011, 2019; Palmeirim et al. 2013; Cox et al. 2016) have found that these filaments are inconsistent with the $p = 4$ scenario, instead preferring much shallower power-law indices ($p = 1.5$–2.5).

The Herschel filaments analyzed in previous work lie *within* the local molecular clouds that we analyze here, persisting at much higher column densities ($N_{H_2} > 10^{22}$ cm^{-2}), and on much smaller scales (widths ≈a few tenths of a parsec, lengths ≈a few parsecs). As such, they are unresolved in the Leike et al. (2020a) 3D dust maps that we analyze. Nevertheless, the same formalism can be applied to the much larger molecular clouds these dense filaments inhabit, as the analytic models are scale-free, and we have shown here that local molecular clouds are well described as cylindrical filaments, even at lower densities ($n < 100$ cm^{-3}), where their aspect ratios are often in excess of 3:1 (see lengths and widths in Tables 1 and 2). Thus, while we target a very different regime—about two orders of magnitude lower in density, and an order of magnitude larger spatial scale—the comparison to the classical $p = 4$ Ostriker (1964) model for an isothermal, self-gravitating filament in hydrostatic equilibrium is still relevant.

We find that the local, large-scale, molecular clouds studied here have shallower radial density profiles, with typical power-law indices p between 1.5 and 2.5, than would an isothermal self-gravitating cylinder in hydrostatic equilibrium. This shallower

power law, while inconsistent with isothermal self-gravitating filaments in the absence of a magnetic field, could be consistent with some models of magnetized filaments (Fiege & Pudritz 2000). Previous studies of the structure of the magnetic field in solar neighborhood clouds have found a strong coupling between the gas column density and the magnetic field orientation, which is consistent with the idea that magnetic fields play an important role in structuring the interstellar medium in and around local molecular clouds (see e.g., Soler 2019).

However, given that the parameters of the Plummer profile are *highly* degenerate (see discussion in Section 4.2), and driven by behavior at the tail of the distribution (at very low densities), we are hesitant to assign any physical significance to the shape of the Plummer profile, other than broadly noting the inconsistency with the Ostriker (1964) result. Similar to the two-component Gaussian results, future comparison with numerical simulations should allow for more robust interpretation of the physical significance, if any, of the shape of the Plummer profiles.

6.3. Comparison between 3D Volume Density and 2D Column Density Radial Profiles

The ultimate goal of this work is to lay the foundation for a robust characterization and interpretation of the structure of molecular clouds. To do so will require the contextualization of these newly presented 3D results with extant 2D approaches. Traditionally, there have been three ways of measuring the column density structure of molecular clouds: near-infrared extinction mapping (e.g., the NICEST method, Section 2.2; Lombardi 2009), thermal dust emission mapping in the far-infrared (e.g., the SFD or Planck dust maps; Schlegel et al. 1998; Planck Collaboration et al. 2016), and spectral-line mapping of CO isotopologues. A systematic analysis of and comparison to the 2D radial profiles of molecular clouds is beyond the scope of this work. So, as a precursor to a more expansive study, we offer in Figure 8 an initial comparison of our 3D radial volume density profile results with traditional 2D column density results for three clouds in the sample (Perseus, Chamaeleon, and Taurus). We compare the 3D radial profiles with three measurements of the 2D radial profile: one obtained from near-infrared extinction using the NICEST maps (see Section 2.2), one obtained from far-infrared dust emission maps (Schlegel et al. 1998), and one obtained by projecting the 3D dust map from Leike et al. (2020a) on to the plane of the sky, using the same column density maps from Section 3.3. Each curve has been smoothed with a kernel roughly equal to 2 pc (the effective spatial resolution of the Leike et al. 2020a dust map), to alleviate noise in the profiles at large radial distances and facilitate comparison between the different tracers.[35] We largely defer comparison to the 2D structure of clouds obtained from velocity-integrated

---

[35] In all three cases, the radial profiles are obtained identically to our 3D results presented in Section 3.2.1, except the threshold for mask (and thus skeleton) creation was defined in 2D column density space as opposed to 3D volume density space. All 2D maps are convolved to the same resolution. The difference in "zero-point" emission and extinction levels in traditional 2D approaches precludes the application of an identical column density threshold for all three column density maps. To avoid biases in our analysis, we define thresholds using the total area of the cloud masks, rather than absolute column density. That is, we adopt the same $A_K = 0.1$ mag threshold (converted to N_H) used in the Section 3.4 NICEST results to define the optimal mask, and set the thresholds for the 2D dust emission (Schlegel et al. 1998) and projected Leike et al. (2020a) 2D results so they occupy approximately the same area. By doing so, all masks are defined using a narrow range in column density, spanning $N = 1$–3×10^{21} cm^{-2}. A tutorial for how to build 2D radial column density profiles with the `RadFil` package is available on Zenodo (Zucker & Chen 2018b).
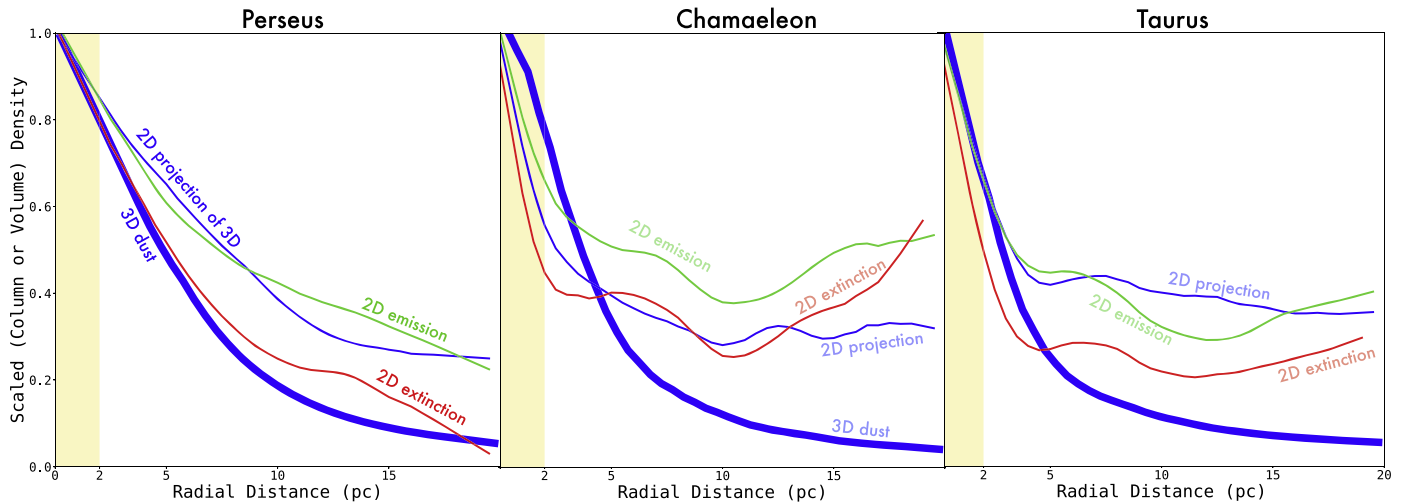
Figure 8. Comparison between 2D radial column density profiles and 3D radial volume density profiles for the Perseus (left panel), Chamaeleon (middle panel) and Taurus (right panel) molecular clouds. The thick blue lines show 3D volume density derived from the Leike et al. (2020a) 3D dust map. The thin blue lines show 2D column density profiles derived by projecting the Leike et al. (2020a) 3D dust map on to the plane of the sky (Section 3.3). The red lines show 2D column density from the NICEST map (Lombardi 2009). The green lines show profiles derived from 2D dust emission maps (Schlegel et al. 1998). All maps have been scaled to a peak value of 1.0, to facilitate a comparison of the shapes of the volume and column density profiles. While the 2D and 3D results largely agree at radial distances <5 pc, significant deviations are observed at larger radial distances, particularly for the Chamaeleon and Taurus clouds.

spectral-line maps to future work, given the need for careful accounting of opacity effects and the presence of CO-dark gas. In order to facilitate a comparison of the *shapes* of the profiles, we scale the radial volume density profile and the three radial column density profiles to a peak value of one.

In contrast to the 3D radial profiles, the 2D radial profiles show a much larger variation in structure both within and between clouds. In general, we find good agreement between 2D and 3D results at small radial distances ($r < 5$ pc), particularly for the Perseus and Taurus clouds. However, at radial distances >5 pc, we observe a flattening of the 2D radial profiles that does not manifest in 3D. These larger radial distances are beyond the $A_K = 0.1$ mag boundary used to validate the 3D-dust-based cloud masses in Section 4.4. We observe flattening at large radii even in the projected dust map from Leike et al. (2020a) (thin blue trace), which makes use of the same data as the 3D radial profile (thick blue trace), but simply integrates along the line of sight. The flattening seen (only) in 2D suggests two underlying causes. First, diffuse dust unassociated with (but potentially in the same general vicinity of) the cloud could be contaminating the inferred radial profiles at large radial distances. Second, projection effects intrinsic to the cloud itself (e.g., due to the cloud's orientation with respect to the observer) could be driving this variation. In either or both scenarios, discrepancy between 2D and 3D cloud structure will have profound implications for interpreting the shapes of the column density PDFs of molecular clouds (see Alves et al. 2017; Chen et al. 2019). These deviations also underline the difficulty of validating the atomic outer envelopes of clouds and the tails of the Plummer profiles (Section 6.2) using traditional 2D dust maps. Disentangling these effects will require careful calibration of 2D dust extinction and emission maps; careful supplementation of the 2D dust information with opacity-corrected spectral line maps of CO, H I, and [C II], and contextualization of both types of data in light of synthetic observations of local cloud analogs.

7. Conclusion

The rise of Gaia has transformed our understanding not just of the 3D distribution of stars, but also of the 3D distribution of dust that reddens their colors. The recent release of the Leike et al. (2020a) 3D dust map, which provides 1 pc spatial resolution out to a distance of several hundred parsecs, offers an unprecedented opportunity to measure and describe the shape and internal structure of local molecular clouds on scales previously obtainable only in simulations. Converting from differential dust extinction in the Gaia *G*-band to volume density using a wavelength-dependent extinction curve, we characterize the shapes and thicknesses of famous local clouds in 3D gas density space for the first time. Local clouds appear filamentary, even at gas densities $n < 100\,\mathrm{cm}^{-3}$. Thus, we start by extending the FilFinder algorithm—originally applied to 2D maps of dust emission (Koch & Rosolowsky 2015)—into 3D, to determine the skeletons of nearby clouds, equivalent to a one-voxel-wide representation of their 3D structure. We then extend the RadFil algorithm (Zucker & Chen 2018a) to measure the radial volume density profiles with respect to the cloud spines. Our results are as follows.

1. By projecting each cloud's skeleton—determined in 3D (x, y, z) cartesian space—back to sky coordinates (l, b, d), we constrain the distances to famous local molecular clouds. The 1 pc uncertainty on the distances allows for complete characterization of distance gradients and the presence of multiple components.
2. We model each cloud's radial volume density profile with three functions: a two-component Gaussian, a single-component Gaussian, and a Plummer-like function. Comparing the relative quality of models, we find that a single-component Gaussian function is universally disfavored, with significantly worse odds compared with the two-component Gaussian and Plummer models.
3. For the two-component Gaussian model, we find widths σ_2 of the "outer" Gaussian between 8 and 18 pc, with

amplitudes between $n = 5$ and 15 cm^{-3}. For the "inner" Gaussian, we find widths σ_1 of 2.5–4.9 pc, with amplitudes between $n = 25$ and 52 cm^{-3}. The typical ratio of the outer to inner widths is 3.4: 1, with relatively small scatter (<1). We hypothesize that the boundary might represent a chemical transition between H I and H$_2$ gas in local clouds, with the inner regions probing warm, diffuse molecular gas, and the outer regions tracing the extended atomic envelopes. Another plausible scenario includes a thermal transition between the UNM and the CNM. Future comparison with numerical simulations (e.g., Smith et al. 2020) will be needed to verify these hypotheses.

4. We produce synthetic 2D dust extinction maps (A_K) by projecting the Leike et al. (2020a) 3D dust distribution on the plane of the sky. We compare the 2D extinction maps derived from 3D dust with traditional integrated 2D dust extinction maps (from the NICEST algorithm; Lombardi 2009). Computing cloud masses, we determine that the Leike et al. (2020a) map is recovering a majority of each cloud's mass. However, the 3D dust is insensitive to structure above $A_K = 0.3$ mag ($A_V = 3$ mag).

5. All data underpinning this work are publicly available online at the Harvard Dataverse (https://dataverse.harvard.edu/dataverse/3D_cloud_structure/). An online gallery of interactive figures illustrating our cloud results is also available online here.[36]

Ultimately, these results are only the beginning of what is possible through the combination of Gaia astrometry, large photometric surveys, innovative computational and statistical techniques, and exploratory 3D data visualization. The quality of the Leike et al. (2020a) 3D dust map, and of similar maps extending out many more kiloparsecs (Green et al. 2019; Zucker et al. 2020), relies on accurate measurements of the distance and integrated extinction to individual stars. Not only will future Gaia data releases produce increasingly better estimates of stellar distance, but upcoming photometric surveys like the Vera C. Rubin Observatory Legacy Survey of Space and Time (LSST) will allow for improved constraints on the integrated extinction.

Future 3D dust maps, built on much larger catalogs of stellar properties (e.g., the brutus algorithm; J. S. Speagle et al. 2021, in preparation) should allow for improved models of the 3D dust distribution, probing not only clouds at larger distances, but also with improved sensitivity to higher densities within molecular clouds.

Appendix A
Radial Profiles for Full Cloud Sample

In Figure 3, we present the radial density profiles for two clouds in the sample—Perseus and Chamaeleon. In Figures A1–A3, we show the same radial density profiles for the remaining nine clouds.

---

[36] https://faun.rc.fas.harvard.edu/czucker/Paper_Figures/3D_Cloud_Topologies/gallery.html
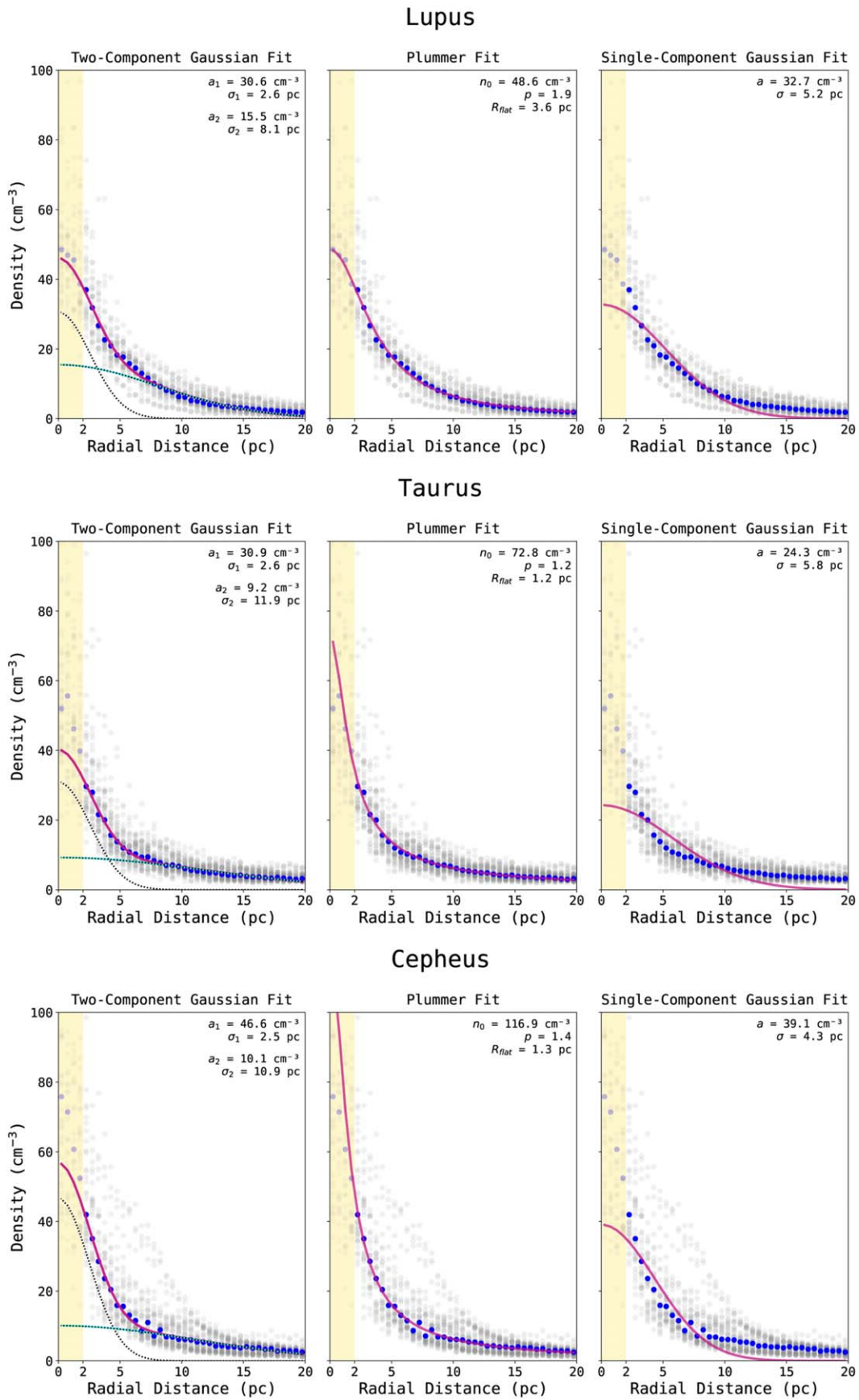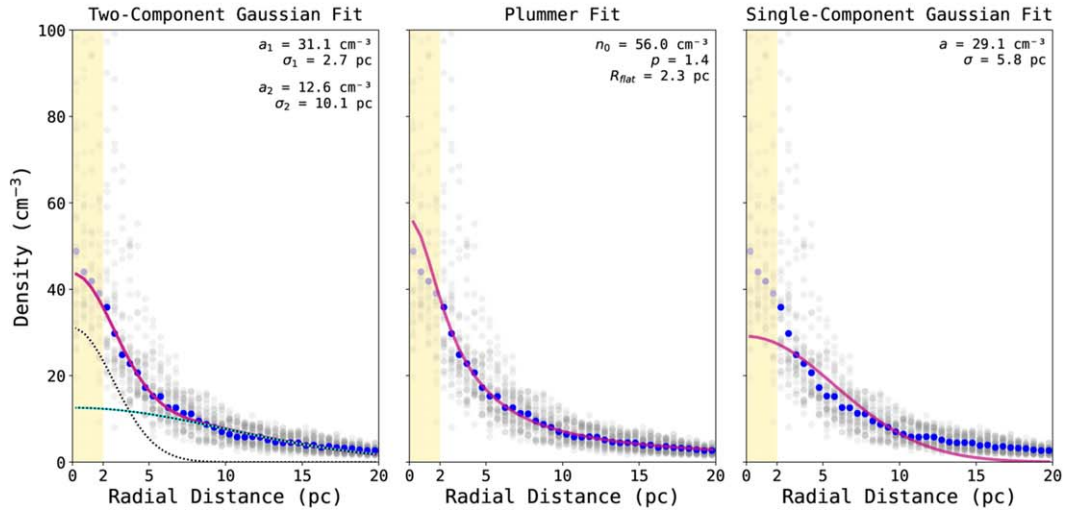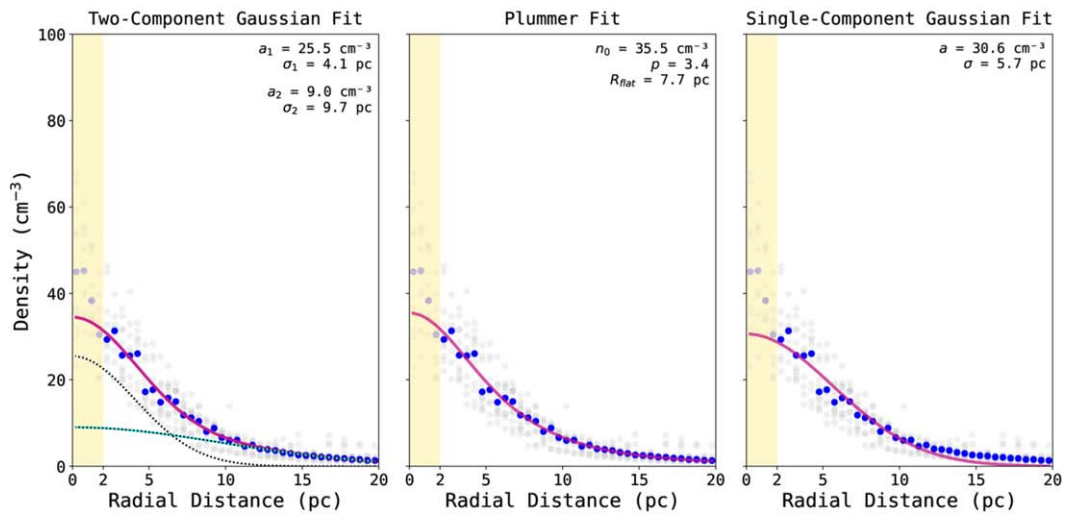
Lupus

Taurus

Cepheus

Figure A1. Same as in Figure 3 except for the Lupus molecular cloud (top row), the Taurus molecular cloud (middle row), and the Cepheus molecular cloud (bottom row).
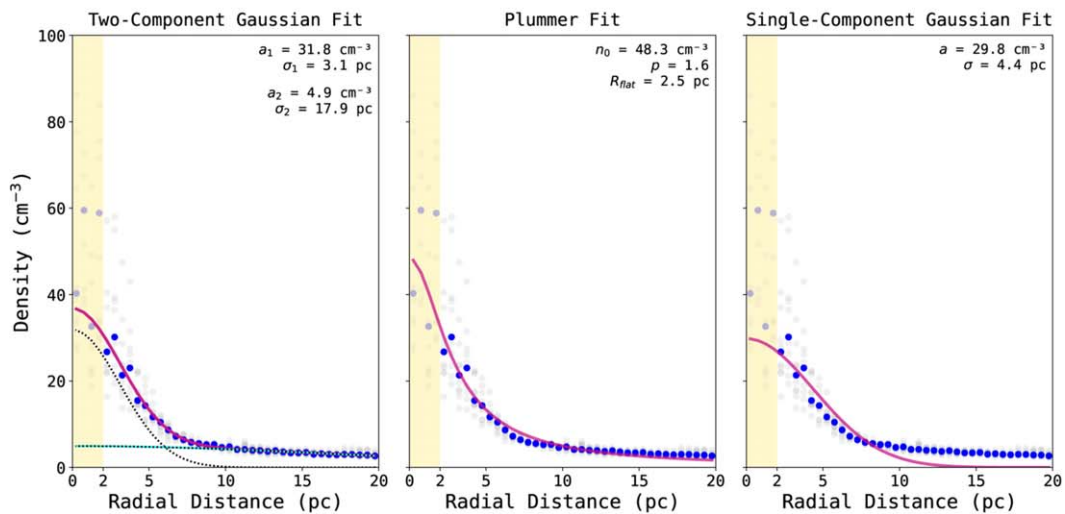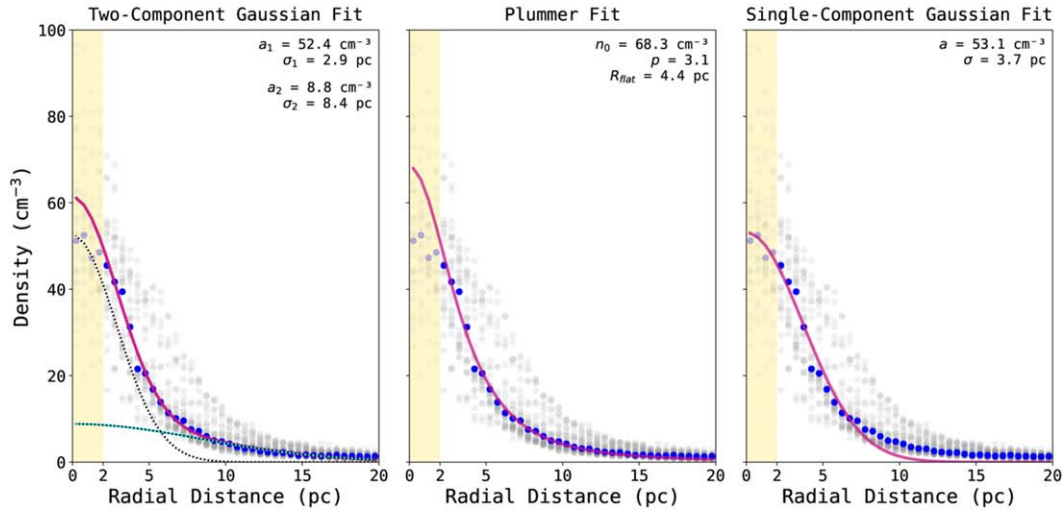
Figure A2. Same as in Figure 3 except for the Ophiuchus molecular cloud (top row), the Pipe nebula (middle row), and the Musca dark cloud (bottom row).
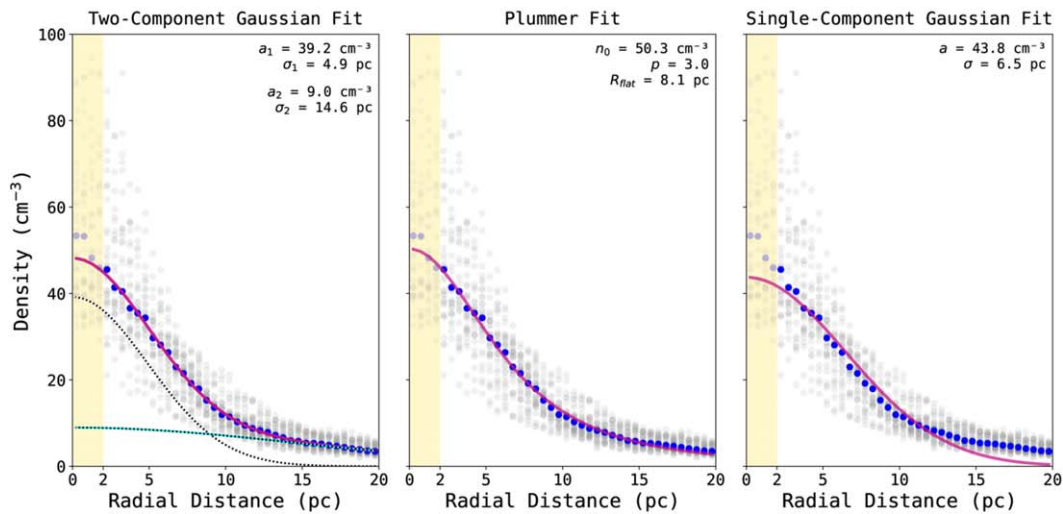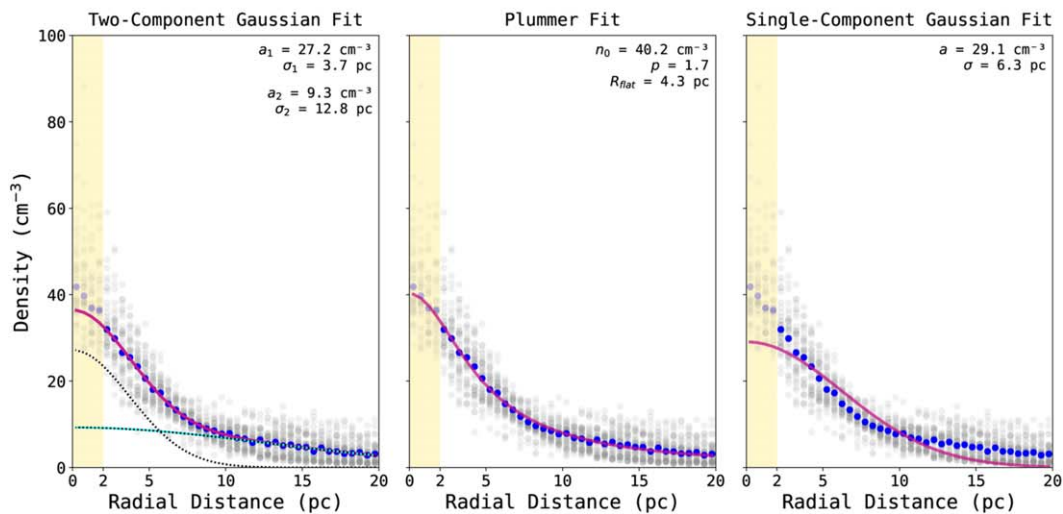
Figure A3. Same as in Figure 3 except for the Orion A molecular cloud (top row), the Orion B molecular cloud (middle row), and the λ Orionis molecular cloud (bottom row). These clouds are at the edge of the Leike et al. (2020a) 3D dust grid, so the results should be treated with more caution than our "complete" cloud sample.

Appendix B
Cloud Widths as a Function of Distance

To determine whether the distance of the cloud influences the widths we derive, we plot the four width parameters fitted for in this study (σ_1 and σ_2 from the two-component Gaussian function, R_{flat} from the Plummer function, and σ from the single-component Gaussian) as a function of distance. The results are shown in Figure B1. If distance was influencing the cloud widths, we would expect the cloud widths to increase as a function of distance. As we show in Figure B1, we find no such correlation, indicating that the cloud distance is not strongly biasing our results.
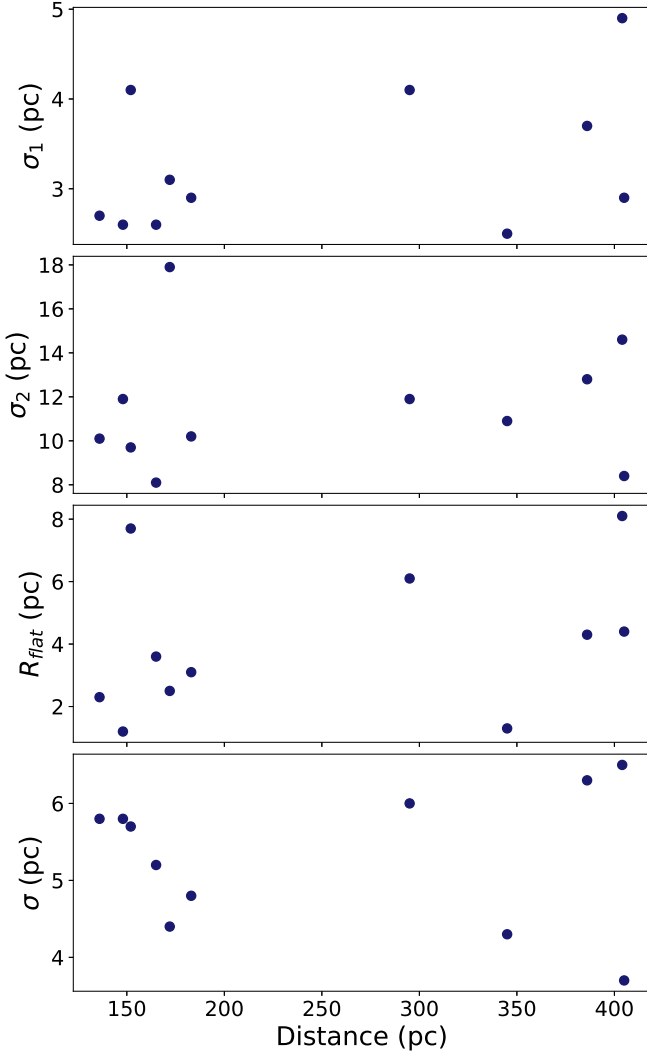
Figure B1. Derived width parameters as a function of cloud distance, with the "inner" width σ_1 of the two-component Gaussian fit, the "outer" width σ_2 of the two-component Gaussian fit, the flattening radius R_{flat} of the Plummer fit, and the standard deviation σ of the single-component Gaussian fit shown from top to bottom.

Appendix C
Comparison between 3D Dust Correlation Kernel and Measured Profiles

In this section, we compare the shape of the correlation kernel of the Leike et al. (2020a) 3D dust reconstruction with the shape of our cloud profiles. Our goal is to determine the extent to which our cloud profiles are driven by data local to the cloud, versus the prior on the dust extinction density. Leike et al. (2020a) assumed the prior on the dust extinction density s_x to be positive and spatially correlated, enforced via a log-normal Gaussian process prior of the form

$$s_x = \rho_0 \exp(\tau_x)$$
$$\tau \curvearrowleft \mathcal{G}(\tau | 0, T)$$

where ρ_0 is the prior median extinction density and T is the correlation kernel of the Gaussian Process τ_x. The ρ_0 term is a hyperparameter of the model, and is set to $\rho_0 = \frac{1}{1000\,\mathrm{pc}^{-1}}$. The correlation kernel T is inferred during their reconstruction. To parallelize the reconstruction, Leike et al. (2020a) split the local volume into eight octants, with the correlation kernel inferred on an octant by octant basis. We take samples of the correlation kernel inferred for the octant in which each cloud resides, which is equivalent to obtaining samples of the two-point correlation matrix of the logarithmic dust density. The two-point correlation matrix directly indicates how the density at one point is correlated with another point in 3D space.

To facilitate a comparison between the two-point correlation matrix and our profiles, we compute the correlation of each measured profile $C_p(r)$. Before doing so, we convert the radial profiles as a function of gas density $n(r)$, utilized throughout this study, back to the native units of the Leike et al. (2020a) 3D dust map, by dividing each profile by a factor of 880 (see Section 2) to obtain $s_x(r)$. Because the two-point correlation matrix describes the logarithmic dust density, rather than the dust density, we further transform $s_x(r)$ into logarithmic density space, hereafter $p(r)$:

$$p(r) = \log(s_x(r) \times 1000) \tag{C1}$$

where the factor of 1000 accounts for the scaling of the hyperparameter ρ_0. To calculate the correlation of the profile $C_p(r)$, we compute

$$C_p(r) = p(r) \times p(0) \tag{C2}$$

where $p(0)$ is the logarithmic density of the radial profile in Equation (C1) at a radial distance of 0 pc. Given the overdensity of the dust at $r = 0$ pc, this comparison describes how much of the dust at larger radial distances can be explained by the correlation kernel of the dust map. In Figure C1 we plot T versus $C_p(r)$ for each cloud, where T constitutes samples of two-point correlation matrix inferred in the cloud's octant, and $C_p(r)$ is the correlation of the profile we
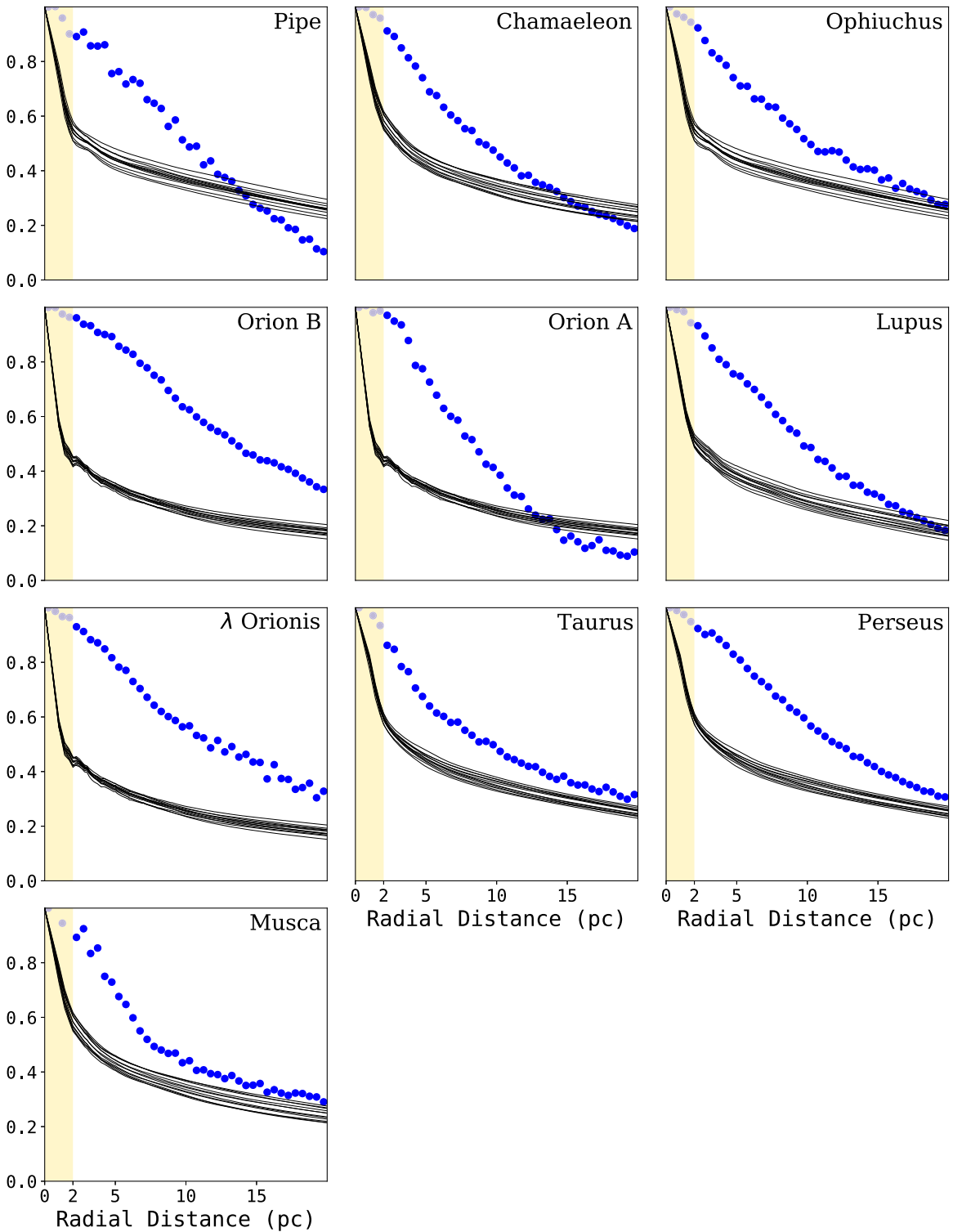
Figure C1. Comparison between samples of the two-point correlation function derived from the Leike et al. (2020a) 3D dust kernel (black lines) and the derived correlation of each cloud's radial profile obtained in this work (blue points). Both the 3D dust map's correlation kernel and correlation of the cloud radial profiles have been scaled to a peak value of one. At smaller radial distances, our measured profiles deviate significantly from the underlying correlation kernel used to derive the map, indicating that the inner widths that we obtain for the clouds are robust. However, at larger radial distances, the shape of the kernel and profiles become similar, indicating that the dust at larger radial distances may be prior-dominated. However, as the prior is inferred using real cloud structure, the outer envelopes could still be physically meaningful. See Appendix C for full details.

construct in Section 3.2.1. We normalize both T and $C_p(r)$ to a peak value of 1.0.

We observe that the shape of $C_p(r)$ and T are qualitatively different between radial distances of 2 and 10 pc, indicating that the "inner" widths of our two-component Gaussian results

are driven by data local to the cloud, rather than the kernel used in the 3D dust's reconstruction. However, for radial distances >10 pc, we see the slopes of $C_p(r)$ and T become increasingly similar, particularly for the Musca, Taurus, Ophiuchus, and Orion A clouds. The similarity between the shape of $C_p(r)$ and

T at larger radial distances could indicate that the kernel is driving the structure of clouds at lower densities. However, because the kernel is inferred using data inclusive of the cloud's structure (in addition to structure beyond each cloud of interest) the outer envelopes could still be physically meaningful. More validation in future work will be needed to fully verify the relationship, if any, between the outer envelopes we observe in our radial profiles and the atomic gas envelopes of local molecular clouds, as discussed in Section 6.

Appendix D
Radial Profile Fitting Results for the Full Profile

In Section 4, we discuss the width results where the inner profiles (radial distances <2 pc) are excluded from the fit, due to the Leike et al. (2020a) map's 1 pc grid and its caveat that features less than 2 pc in size should be treated with caution. For completeness, in Table D1 we report the results of the full profile fits, including radial distance bins between 0 and 20 pc.

In general, we find that including the inner 2 pc of each radial profile in the fit has a modest effect on the model parameters. When including the inner 2 pc for the two-component Gaussian fit (in comparison to the results from Section 4), the inner width σ_1 changes on average by 15%, while the outer width typically differs by 17%. For the single-component Gaussian, σ differs on average by 20%. We see the largest difference in the Plummer model, with $R_{\rm flat}$ changing by 28% on average. Overall, however, the quality of all model fits decreases when including the inner 2 pc, which is why we report the results excluding the inner 2 pc, over the full profile results, in the main text. The decline in the quality of the fit, as determined using the same procedure outlined in Section 4.2.1, is consistent with our understanding that the Leike et al. (2020a) dust map is unreliable at scales <2 pc, and is also less accurate at reconstructing the highest gas densities, which are closest to the spine. Thus, it is not surprising that the fit improves when only higher fidelity measurements, farther from the spine, are included.

Table D1
Radial Volume Density Fitting (Full Profile)

Cloud	Two-Component Gaussian							Plummer					Single Gaussian			
	σ_1 (pc)	a_1 (cm^{-3})	σ_2 (pc)	a_2 (cm^{-3})	$\sigma_{n,\mathrm{G2}}^2$ (cm^{-3})	$\frac{\sigma_2}{\sigma_1}$	lnZ_{G2}	n_0 (cm^{-3})	R_{flat} (pc)	p	$\sigma_{n,\mathrm{P}}^2$ (cm^{-3})	$\ln Z_{\mathrm{P}}$	σ (pc)	a (cm^{-3})	$\sigma_{n,\mathrm{G1}}^2$ (cm^{-3})	$\ln Z_{\mathrm{G1}}$
(1)	(2)	(3)	(4)	(5)	(6)	(7)	(8)	(9)	(10)	(11)	(12)	(13)	(14)	(15)	(16)	(17)
Chamaeleon	$2.6^{+0.1}_{-0.1}$	$34.5^{+0.7}_{-0.7}$	$9.4^{+0.5}_{-0.4}$	$10.2^{+0.7}_{-0.7}$	$0.4^{+0.1}_{-0.1}$	3.6	-19.7	$46.1^{+0.3}_{-0.3}$	$3.4^{+0.1}_{-0.1}$	$1.9^{+0.1}_{-0.1}$	$0.3^{+0.1}_{-0.1}$	-10.8	$3.8^{+0.2}_{-0.2}$	$41.1^{+1.6}_{-1.6}$	$10.0^{+2.8}_{-2.0}$	-73.1
Ophiuchus	$2.4^{+0.1}_{-0.1}$	$33.1^{+0.9}_{-1.0}$	$9.6^{+0.5}_{-0.5}$	$13.6^{+1.0}_{-0.9}$	$0.9^{+0.3}_{-0.2}$	3.9	-33.8	$48.1^{+0.5}_{-0.5}$	$2.9^{+0.1}_{-0.1}$	$1.5^{+0.0}_{-0.0}$	$0.5^{+0.1}_{-0.1}$	-22.6	$4.3^{+0.3}_{-0.3}$	$40.6^{+2.2}_{-2.0}$	$16.9^{+4.9}_{-3.5}$	-82.3
Lupus	$2.3^{+0.1}_{-0.1}$	$31.4^{+1.3}_{-1.3}$	$7.7^{+0.4}_{-0.3}$	$17.1^{+1.3}_{-1.4}$	$1.0^{+0.3}_{-0.2}$	3.3	-34.3	$49.0^{+0.5}_{-0.5}$	$3.6^{+0.2}_{-0.2}$	$1.9^{+0.1}_{-0.1}$	$0.5^{+0.2}_{-0.1}$	-24.6	$4.2^{+0.2}_{-0.2}$	$42.9^{+1.8}_{-1.7}$	$12.1^{+3.4}_{-2.5}$	-76.6
Taurus	$2.0^{+0.1}_{-0.1}$	$43.1^{+1.0}_{-1.1}$	$10.4^{+0.8}_{-0.7}$	$11.2^{+0.9}_{-0.9}$	$1.8^{+0.5}_{-0.3}$	5.2	-45.3	$56.8^{+1.0}_{-1.0}$	$1.9^{+0.1}_{-0.1}$	$1.4^{+0.1}_{-0.1}$	$1.8^{+0.5}_{-0.4}$	-46.0	$3.1^{+0.3}_{-0.2}$	$48.2^{+3.2}_{-3.0}$	$24.4^{+7.1}_{-5.0}$	-89.3
Perseus	$3.3^{+0.2}_{-0.2}$	$35.0^{+1.9}_{-1.9}$	$9.7^{+0.8}_{-0.6}$	$16.5^{+2.0}_{-2.0}$	$1.8^{+0.5}_{-0.4}$	3.0	-45.0	$52.5^{+0.6}_{-0.6}$	$4.8^{+0.3}_{-0.3}$	$2.0^{+0.1}_{-0.1}$	$1.1^{+0.3}_{-0.2}$	-37.3	$5.2^{+0.2}_{-0.2}$	$46.8^{+1.5}_{-1.5}$	$13.6^{+3.7}_{-2.8}$	-79.0
Musca[a]	$2.6^{+0.3}_{-0.2}$	$42.8^{+3.1}_{-3.5}$	$14.7^{+6.1}_{-4.9}$	$6.1^{+2.6}_{-1.7}$	$23.6^{+6.8}_{-4.5}$	5.7	-89.0	$49.9^{+3.2}_{-3.3}$	$3.9^{+1.6}_{-1.0}$	$2.6^{+1.4}_{-0.7}$	$26.2^{+7.5}_{-5.4}$	-91.4	$3.2^{+0.3}_{-0.3}$	$46.7^{+3.3}_{-3.3}$	$33.6^{+10.0}_{-6.7}$	-95.7
Pipe	$2.6^{+0.3}_{-0.2}$	$24.4^{+2.4}_{-1.8}$	$7.6^{+0.6}_{-0.4}$	$18.1^{+1.4}_{-2.8}$	$4.0^{+1.1}_{-0.9}$	2.9	-58.3	$42.0^{+1.2}_{-1.2}$	$4.8^{+0.7}_{-0.6}$	$2.2^{+0.4}_{-0.3}$	$3.8^{+1.1}_{-0.8}$	-57.2	$4.9^{+0.2}_{-0.2}$	$37.4^{+1.4}_{-1.4}$	$10.4^{+2.9}_{-2.2}$	-73.6
Cepheus	$2.0^{+0.1}_{-0.1}$	$60.6^{+1.3}_{-1.3}$	$9.1^{+0.7}_{-0.6}$	$13.5^{+1.2}_{-1.1}$	$2.1^{+0.6}_{-0.4}$	4.6	-48.2	$77.9^{+0.8}_{-0.7}$	$2.1^{+0.1}_{-0.1}$	$1.6^{+0.0}_{-0.0}$	$0.8^{+0.2}_{-0.2}$	-32.9	$2.8^{+0.2}_{-0.2}$	$67.9^{+3.1}_{-3.1}$	$28.3^{+8.2}_{-5.9}$	-92.3
Orion A[b]	$3.3^{+0.1}_{-0.1}$	$48.6^{+1.4}_{-2.0}$	$11.2^{+3.9}_{-2.2}$	$5.0^{+2.0}_{-1.5}$	$2.4^{+0.7}_{-0.5}$	3.4	-48.6	$54.2^{+1.0}_{-1.0}$	$7.0^{+0.7}_{-0.7}$	$4.8^{+0.7}_{-0.7}$	$3.3^{+0.9}_{-0.7}$	-54.3	$3.7^{+0.1}_{-0.1}$	$52.4^{+1.1}_{-1.1}$	$5.4^{+1.7}_{-1.1}$	-62.8
Orion B[b]	$4.5^{+0.2}_{-0.2}$	$38.1^{+2.1}_{-2.3}$	$12.0^{+1.6}_{-1.1}$	$12.6^{+2.4}_{-2.3}$	$1.2^{+0.3}_{-0.2}$	2.7	-36.5	$51.6^{+0.5}_{-0.5}$	$7.5^{+0.4}_{-0.4}$	$2.8^{+0.2}_{-0.2}$	$1.0^{+0.3}_{-0.2}$	-34.7	$6.0^{+0.2}_{-0.2}$	$47.8^{+1.2}_{-1.1}$	$8.7^{+2.4}_{-1.7}$	-70.5
λ Orionis[b]	$3.3^{+0.1}_{-0.1}$	$28.9^{+0.8}_{-0.8}$	$11.6^{+0.7}_{-0.6}$	$10.9^{+0.8}_{-0.8}$	$0.5^{+0.2}_{-0.1}$	3.5	-23.7	$41.0^{+0.4}_{-0.4}$	$4.1^{+0.2}_{-0.2}$	$1.7^{+0.1}_{-0.1}$	$0.4^{+0.1}_{-0.1}$	-17.5	$5.2^{+0.3}_{-0.3}$	$35.9^{+1.5}_{-1.5}$	$11.1^{+3.2}_{-2.2}$	-74.6

Notes. Radial density profile fitting results for local clouds, computed over radial distances between 0 and 20 pc. Unlike Table 2, we do not exclude the inner 2 pc from the fit. (1) Name of the cloud. (2–6) Best-fit parameters for the two-component Gaussian fit, including the standard deviation and amplitude of the narrower Gaussian (σ_1, a_1), the standard deviation and amplitude of the broader Gaussian (σ_2, a_2), and the square of the modeled scatter in the density measurements ($\sigma_{n,\mathrm{G2}}^2$). (7) Ratio of the outer to inner Gaussian standard deviations. (8) Logarithm of the evidence of the two-component Gaussian fit. (9–12) Best-fit parameters of the Plummer fit, including the peak amplitude n_0, the flattening radius R_{flat}, the power index of the density profile p, and the square of the modeled scatter in the density measurements ($\sigma_{n,\mathrm{P}}^2$). (13) Logarithm of the evidence of the Plummer fit. (14–16) Standard deviation σ, amplitude a, and the square of the modeled scatter in the density measurements ($\sigma_{n,\mathrm{G1}}^2$) for the single-component Gaussian fit. (17) Logarithm of the evidence of the single-component Gaussian fit. We report the single-component Gaussian results here for completeness only, as it is a poor fit to the data particularly at large radial distances. A machine readable version of this table is available at https://doi.org/10.7910/DVN/V8NGLX.

[a] At small radial distances, Musca is largely unresolved in the Leike et al. (2020a) map, and at large radial distances, its structure is consistent with being prior-dominated, so we urge caution when interpreting the results.

[b] Clouds below the horizontal line—Orion A, Orion B, and λ Orionis—should be treated with caution, as they lie at the very edge of the Leike et al. (2020a) 3D dust grid and are subjected to additional biases. Part of Orion A, toward the Orion Nebula Cluster, is also devoid of dust in the Leike et al. (2020a) 3D dust map despite being highly extinguished. See Section 5 for full details.

Appendix E
Radial Profile Fitting Results Using Samples of the 3D Dust Map

In deriving their 3D dust map, Leike et al. (2020a) generated 12 posterior samples, or realizations, of the extinction density, and the 3D dust map derived from the mean of these posterior samples is used in the fitting results reported in Section 4. However, because the uncertainty in the underlying 3D dust reconstruction is not accounted for when characterizing the radial profiles, it is necessary to quantify how much our results change when different realizations of the 3D dust distribution are used, rather than just the mean. To do so, we create a new likelihood function, building on the formalism described in Section 3.2.2. Recall that when fitting 3D dust determined by the mean of the samples, we adopt a Gaussian log-likelihood that takes the following form:

$$\mathcal{L}_{\mathrm{mean}} = \ln p(n\,|\,\theta,\,\sigma_n^2) = -\frac{1}{2}\sum_i\left[\frac{(n_i - n_{\theta,i})^2}{\sigma_n^2} + \ln(2\pi\sigma_n^2)\right]$$
(E1)

where n_i is the measured profile in the ith radial distance bin characterized by the mean 3D dust map, $n_{\theta,i}$ is the model density profile in the ith distance bin (for the single Gaussian, two-component Gaussian, or Plummer fit), θ constitutes the parameters characterizing the model density profile for each fit (e.g., σ, a for the single Gaussian fit), and σ_n^2 is the square of the scatter in the density (across all bins) that we infer as part of our modeling.

Our new likelihood function, taking into account all 12 realizations of the 3D dust map, is of the form

$$\mathcal{L}_{\mathrm{samples}} = \ln[\exp(\mathcal{L}_{\mathrm{sample}_1}) + \exp(\mathcal{L}_{\mathrm{sample}_2})$$
$$+ \ldots + \exp(\mathcal{L}_{\mathrm{sample}_{12}})] - \ln(12)$$
(E2)

where L_{sample_1} is calculated equivalently to L_{mean}, except the measured radial density profile n is derived from the 1st sample of the 3D dust map. There are 12 samples, so we compute the radial profile for each, assuming the same filament spine as determined for the mean dust map. We exclude the inner 2 pc of the radial profiles when fitting, as we do for the results reported in Table 2. Each of the 12 samples is a possible reality with a probability of $\frac{1}{12}$, and therefore the combined probability is their average. Thus, the total log-likelihood is the average of the individual likelihoods derived from each realization. We sample for the best-fit model parameters for all three functions (single-component Gaussian, two-component Gaussian, Plummer) for all clouds, using the same priors and the same dynesty nested sampling framework that we employ in Section 3.2.2. Our results are summarized in Table E1.

Overall, we find that that uncertainty in the profile fitting derived from the uncertainty in the 3D dust map has only a modest effect on our results. For the two-component Gaussian, the typical percent difference between the sample-based inference and the mean-based inference is 2% for σ_2, 10% for σ_1, 21% for a_2 and 11% for a_1. For the Plummer fit, p changes by an average of 8%, n_0 by 17%, and R_{flat} by 22%. However, we do note that for three clouds—Pipe, λ Orionis, and Musca, the R_{flat} parameter changes more drastically, increasing by a factor of two when using the 3D dust samples rather than the mean. This larger change could be tied to the degeneracy in the Plummer modeling described in Section 4.3, which provides another reason not to over-interpret the Plummer models, as we caution in Section 6.2. The two-component Gaussian fit is much more robust, and the sample-based fitting results reported in Table E1 do not affect any physical interpretation of the profile shapes described in Section 6.

Table E1
Radial Volume Density Fitting (Computed Using All Realizations of 3D Dust Map)

	Two-Component Gaussian							Plummer					Single Gaussian			
Cloud	σ_1 (pc)	a_1 (cm^{-3})	σ_2 (pc)	a_2 (cm^{-3})	$\sigma^2_{n,\mathrm{G2}}$ (cm^{-3})	$\frac{\sigma_2}{\sigma_1}$	$\ln Z_{\mathrm{G2}}$	n_0 (cm^{-3})	R_{flat} (pc)	p	$\sigma^2_{n,\mathrm{P}}$ (cm^{-3})	$\ln Z_{\mathrm{P}}$	σ (pc)	a (cm^{-3})	$\sigma^2_{n,\mathrm{G1}}$ (cm^{-3})	$\ln Z_{\mathrm{G1}}$
(1)	(2)	(3)	(4)	(5)	(6)	(7)	(8)	(9)	(10)	(11)	(12)	(13)	(14)	(15)	(16)	(17)
Chamaeleon	$2.8^{+0.1}_{-0.1}$	$29.2^{+0.7}_{-0.6}$	$10.4^{+0.4}_{-0.3}$	$8.0^{+0.4}_{-0.4}$	$0.1^{+0.0}_{-0.0}$	3.7	-4.1	$46.9^{+1.7}_{-1.9}$	$2.6^{+0.2}_{-0.1}$	$1.7^{+0.1}_{-0.0}$	$0.1^{+0.0}_{-0.0}$	0.3	$4.7^{+0.4}_{-0.4}$	$28.3^{+3.7}_{-2.3}$	$4.8^{+1.6}_{-1.1}$	-55.7
Ophiuchus	$2.7^{+0.1}_{-0.1}$	$34.0^{+1.2}_{-1.5}$	$10.9^{+0.5}_{-0.5}$	$10.3^{+0.6}_{-0.6}$	$0.4^{+0.1}_{-0.1}$	4.1	-19.7	$56.6^{+2.7}_{-2.5}$	$2.3^{+0.2}_{-0.1}$	$1.4^{+0.0}_{-0.0}$	$0.2^{+0.1}_{-0.0}$	-8.2	$5.2^{+0.5}_{-0.4}$	$28.7^{+2.3}_{-2.3}$	$7.9^{+2.4}_{-1.8}$	-63.0
Lupus	$3.5^{+0.2}_{-1.4}$	$27.6^{+14.6}_{-1.4}$	$10.0^{+1.3}_{-1.4}$	$9.4^{+4.0}_{-1.8}$	$0.4^{+0.1}_{-0.1}$	2.9	-19.5	$42.3^{+11.7}_{-3.8}$	$3.5^{+1.3}_{-0.9}$	$1.8^{+0.4}_{-0.2}$	$0.3^{+0.1}_{-0.1}$	-13.3	$5.4^{+0.3}_{-0.2}$	$29.5^{+1.4}_{-1.5}$	$4.2^{+1.2}_{-1.0}$	-54.0
Taurus	$2.3^{+0.1}_{-0.1}$	$36.2^{+1.2}_{-1.5}$	$11.5^{+0.6}_{-0.4}$	$8.7^{+0.3}_{-0.4}$	$0.2^{+0.1}_{-0.0}$	5.0	-9.7	$54.4^{+7.2}_{-4.7}$	$1.6^{+0.2}_{-0.2}$	$1.3^{+0.0}_{-0.0}$	$0.2^{+0.1}_{-0.0}$	-10.2	$5.2^{+0.7}_{-0.7}$	$24.0^{+4.1}_{-2.8}$	$7.9^{+2.4}_{-1.8}$	-63.0
Perseus	$3.7^{+0.1}_{-0.1}$	$26.3^{+0.9}_{-0.9}$	$11.4^{+0.7}_{-0.6}$	$11.5^{+1.0}_{-1.0}$	$0.4^{+0.1}_{-0.1}$	3.1	-20.3	$40.8^{+1.0}_{-0.9}$	$4.7^{+0.3}_{-0.3}$	$1.8^{+0.1}_{-0.1}$	$0.3^{+0.1}_{-0.1}$	-17.5	$6.4^{+0.4}_{-0.6}$	$31.1^{+3.2}_{-1.7}$	$6.1^{+1.9}_{-1.4}$	-59.3
Musca[a]	$2.9^{+0.1}_{-0.1}$	$36.1^{+0.8}_{-0.8}$	$20.9^{+2.7}_{-2.9}$	$3.3^{+0.3}_{-0.2}$	$0.4^{+0.1}_{-0.1}$	7.1	-17.1	$145.3^{+16.9}_{-22.9}$	$1.0^{+0.2}_{-0.1}$	$1.6^{+0.0}_{-0.0}$	$0.5^{+0.2}_{-0.2}$	-24.3	$3.6^{+0.2}_{-0.2}$	$34.5^{+2.7}_{-2.5}$	$5.2^{+1.6}_{-1.1}$	-56.9
Pipe	$2.9^{+0.4}_{-0.2}$	$29.5^{+8.4}_{-9.3}$	$9.9^{+0.8}_{-0.7}$	$8.3^{+1.3}_{-1.1}$	$0.5^{+0.2}_{-0.1}$	3.4	-21.8	$49.5^{+3.4}_{-3.1}$	$2.6^{+0.3}_{-0.2}$	$1.8^{+0.1}_{-0.1}$	$0.3^{+0.1}_{-0.1}$	-16.0	$6.6^{+0.2}_{-0.2}$	$21.8^{+0.8}_{-0.8}$	$2.3^{+0.7}_{-0.5}$	-44.9
Cepheus	$2.8^{+0.1}_{-0.6}$	$41.6^{+8.7}_{-1.4}$	$10.9^{+1.4}_{-1.4}$	$6.7^{+1.9}_{-0.9}$	$0.6^{+0.2}_{-0.1}$	3.9	-25.1	$159.1^{+8.0}_{-12.6}$	$1.0^{+0.1}_{-0.0}$	$1.6^{+0.0}_{-0.0}$	$0.2^{+0.1}_{-0.0}$	-6.5	$3.9^{+0.2}_{-0.2}$	$38.9^{+2.7}_{-2.8}$	$6.5^{+2.1}_{-1.4}$	-61.0
Orion A[b]	$3.1^{+0.2}_{-0.6}$	$48.0^{+19.7}_{-14.4}$	$8.7^{+3.3}_{-1.0}$	$7.0^{+2.3}_{-3.5}$	$0.4^{+0.1}_{-0.1}$	2.8	-18.9	$80.1^{+3.4}_{-34.0}$	$4.2^{+0.6}_{-0.3}$	$3.3^{+0.3}_{-0.4}$	$0.4^{+0.1}_{-0.1}$	-17.7	$3.9^{+0.1}_{-0.1}$	$46.9^{+1.5}_{-1.3}$	$2.1^{+0.6}_{-0.5}$	-43.4
Orion B[b]	$3.8^{+0.1}_{-0.1}$	$35.5^{+1.1}_{-1.2}$	$11.1^{+0.8}_{-0.7}$	$11.7^{+1.3}_{-1.3}$	$0.6^{+0.2}_{-0.1}$	2.9	-25.3	$50.8^{+1.1}_{-1.1}$	$5.4^{+0.3}_{-0.3}$	$2.3^{+0.1}_{-0.1}$	$0.5^{+0.2}_{-0.1}$	-24.4	$6.0^{+0.2}_{-0.2}$	$39.9^{+1.5}_{-1.4}$	$5.0^{+1.6}_{-1.2}$	-57.0
λ Orionis[b]	$3.8^{+0.1}_{-0.1}$	$30.3^{+0.6}_{-0.7}$	$13.9^{+1.6}_{-1.2}$	$5.9^{+0.7}_{-0.6}$	$0.3^{+0.1}_{-0.1}$	3.7	-14.3	$85.1^{+22.9}_{-11.7}$	$1.2^{+0.2}_{-0.3}$	$1.3^{+0.0}_{-0.0}$	$0.2^{+0.1}_{-0.0}$	-8.7	$5.7^{+0.4}_{-0.3}$	$28.0^{+2.7}_{-6.0}$	$3.5^{+1.1}_{-0.8}$	-50.5

Notes. Radial density profile fitting results for local clouds, computed using the likelihood function shown in Equation (E2) and described in Appendix E. The likelihood in Equation (E2) utilizes all realizations of the 3D dust map distribution from Leike et al. (2020a), rather than just the mean distribution, allowing us to quantify the effect of the underlying uncertainty in the 3D dust reconstruction on our results. (1) Name of the cloud. (2–6) Best-fit parameters for the two-component Gaussian fit, including the standard deviation and amplitude of the narrower Gaussian (σ_1, a_1), the standard deviation and amplitude of the broader Gaussian (σ_2, a_2), and the square of the modeled scatter in the density measurements ($\sigma^2_{n,\mathrm{G2}}$). (7) Ratio of the outer to inner Gaussian standard deviations. (8) Logarithm of the evidence of the two-component Gaussian fit. (9–12) Best-fit parameters of the Plummer fit, including the peak amplitude n_0, the flattening radius R_{flat}, the power index of the density profile p, and the square of the modeled scatter in the density measurements ($\sigma^2_{n,\mathrm{P}}$). (13) Logarithm of the evidence of the Plummer fit. (14–16) Standard deviation σ, amplitude a, and the square of the modeled scatter in the density measurements ($\sigma^2_{n,\mathrm{G1}}$) for the single-component Gaussian fit. (17) Logarithm of the evidence of the single-component Gaussian fit. We report the single-component Gaussian results here for completeness only, as it is a poor fit to the data particularly at large radial distances. A machine readable version of this table is available at https://doi.org/10.7910/DVN/94OKZD.
[a] At small radial distances, Musca is largely unresolved in the Leike et al. (2020a) map, and at large radial distances, its structure is consistent with being prior-dominated, so we urge caution when interpreting the results.
[b] Clouds below the horizontal line—Orion A, Orion B, and λ Orionis—should be treated with caution, as they lie at the very edge of the Leike et al. (2020a) 3D dust grid and are subjected to additional biases. Part of Orion A, toward the Orion Nebula Cluster, is also devoid of dust in the Leike et al. (2020a) 3D dust map despite being highly extinguished. See Section 5 for full details.

Appendix F
Comparison to CO Radial Profiles

We build radial profiles of the CO emission in order to test the H I-to-H$_2$ transition hypothesis presented in Section 6.1.1. Specifically, if CO emission is detected significantly beyond the boundaries of the inner Gaussian profile, the two-component Gaussian would not represent a phase transition between atomic and molecular gas, disproving the hypothesis discussed in Section 6.1.1. For this test, we leverage data from the 1.2 m CfA CO survey (Dame et al. 2001), selecting all clouds that have broad enough CO coverage to probe potential emission at large radial distances (seven of 11 clouds in the sample). For each cloud, we produce integrated intensity maps of the ^{12}CO emission over the velocity range of -15 to 15 km s^{-1}. We then smooth each map to the resolution of the Leike et al. (2020a) data at the distance of the cloud (see Table 1) and define 2D masks by thresholding the integrated intensity maps at a level of 10 K km s^{-1}. We then follow the procedure for building radial profiles in 2D space, as presented in Zucker & Chen (2018a), which involves skeletonizing the mask and taking cuts across the spine. We employ the "shift"

option to account for CO emission offset from the main spine, ensuring the emission peaks at a radial distance of zero.

The results are presented in Figure F1. In the top-left corner of Figure F1 we show an example of what the 2D skeletonization of the CO integrated intensity masks looks like for a single cloud in the sample—the Perseus Molecular Cloud. In the subsequent panels of Figure F1, we show normalized CO integrated intensity profiles (blue) alongside the normalized density profiles (black) for the inner Gaussian component based on the 3D dust mapping. Both profiles have been scaled to a peak value of one for comparison purposes. We find no extended CO emission beyond the bounds of the inner Gaussian, with most CO profiles showing smaller widths. The one exception is the Taurus Molecular Cloud, whose CO profile is almost identical to the 3D dust profile out to a radial distance of 5 pc, but also shows a secondary peak at larger radial distances. We find that the secondary peak is entirely due to projection effects, stemming from the two components of Taurus (separated by about 10–15 pc along the line of sight) that project to similar areas on the plane of the sky. Thus, we are unable to disprove the H I-to-H$_2$ transition hypothesis given the results of the CO radial profile analysis.
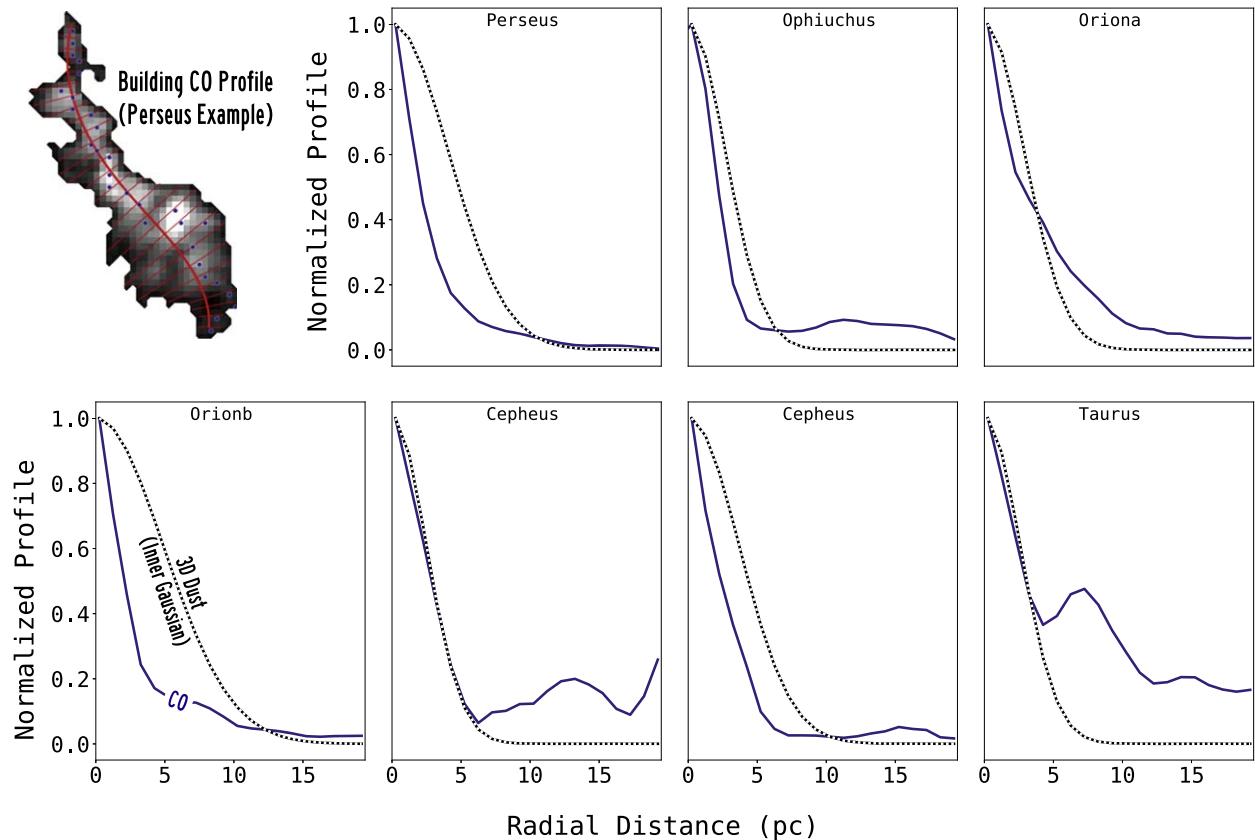
Figure F1. Comparison to CO radial profiles for seven clouds in the sample. The top-left panel shows a schematic for building 2D radial profiles from the ^{12}CO integrated intensity maps for an example cloud (the Perseus Molecular Cloud), including the spine (thick red line), the distribution of integrated CO emission inside the filament mask (background grayscale), the perpendicular cuts across the spine (thin red lines) and the shifted peak integrated emission inside the filament mask (blue points). Note that the radial profiles are measured well beyond the boundaries of the mask, and the mask extent is only used for defining the spine and the optional shifting procedure. The remaining panels show normalized CO integrated intensity radial profiles (navy blue curves) alongside the inner component of the 3D-dust-derived profiles (black dotted curves) for the two-component Gaussian fits presented in the main text. Both components have been normalized to a peak value of one. We find no significant CO emission beyond the boundary of the 3D-dust-derived inner Gaussian profile, finding no direct evidence against the H I-to-H$_2$ transition scenario presented in Section 6.1.1.

ORCID iDs

Catherine Zucker ⓘ https://orcid.org/0000-0002-2250-730X
Alyssa Goodman ⓘ https://orcid.org/0000-0003-1312-0477
João Alves ⓘ https://orcid.org/0000-0002-4355-0921
Shmuel Bialy ⓘ https://orcid.org/0000-0002-0404-003X
Eric W. Koch ⓘ https://orcid.org/0000-0001-9605-780X
Joshua S. Speagle ⓘ https://orcid.org/0000-0003-2573-9832
Michael M. Foley ⓘ https://orcid.org/0000-0002-6747-2745
Douglas Finkbeiner ⓘ https://orcid.org/0000-0003-2808-275X
Reimar Leike ⓘ https://orcid.org/0000-0002-1640-6772
Torsten Enßlin ⓘ https://orcid.org/0000-0001-5246-1624
Joshua E. G. Peek ⓘ https://orcid.org/0000-0003-4797-7030
Gordian Edenhofer ⓘ https://orcid.org/0000-0003-3122-4894

References

Alves, J., Lombardi, M., & Lada, C. J. 2017, A&A, 606, L2
Alves, J., Zucker, C., Goodman, A. A., et al. 2020, Natur, 578, 237
Anders, F., Khalatyan, A., Chiappini, C., et al. 2019, A&A, 628, A94
André, P., Men'shchikov, A., Bontemps, S., et al. 2010, A&A, 518, L102
Arras, P., Frank, P., Leike, R., Westermann, R., & Enßlin, T. A. 2019, A&A, 627, A134
Arzoumanian, D., André, P., Didelon, P., et al. 2011, A&A, 529, L6
Arzoumanian, D., André, P., Könyves, V., et al. 2019, A&A, 621, A42
Astropy Collaboration, Price-Whelan, A. M., Sipőcz, B. M., et al. 2018, AJ, 156, 123
Beaumont, C. N., Offner, S. S. R., Shetty, R., Glover, S. C. O., & Goodman, A. A. 2013, ApJ, 777, 173
Beuther, H., Wang, Y., Soler, J., et al. 2020, A&A, 638, A44
Bialy, S., Bihr, S., Beuther, H., Henning, T., & Sternberg, A. 2017, ApJ, 835, 126
Bialy, S., & Sternberg, A. 2016, ApJ, 822, 83
Bialy, S., Sternberg, A., Lee, M.-Y., Le Petit, F., & Roueff, E. 2015, ApJ, 809, 122
Bokeh Development Team 2018, Bokeh: Python Library for Interactive Visualization, https://bokeh.pydata.org/en/latest/
Busch, M. P., Allen, R. J., Engelke, P. D., et al. 2019, ApJ, 883, 158
Chen, B. Q., Huang, Y., Yuan, H. B., et al. 2019, MNRAS, 483, 4277
Chen, B. Q., Li, G. X., Yuan, H. B., et al. 2020, MNRAS, 493, 351
Cox, N. L. J., Arzoumanian, D., André, P., et al. 2016, A&A, 590, A110
Dame, T. M., Hartmann, D., & Thaddeus, P. 2001, ApJ, 547, 792
Dolan, C. J., & Mathieu, R. D. 2002, AJ, 123, 387
Draine, B. T. 2009, in ASP Conf. Ser. 414, Cosmic Dust—Near and Far, ed. T. Henning, E. Grün, & J. Steinacker (San Francisco, CA: ASP), 453
Duarte-Cabral, A., & Dobbs, C. L. 2016, MNRAS, 458, 3667
Dzib, S. A., Loinard, L., Ortiz-León, G. N., Rodríguez, L. F., & Galli, P. A. B. 2018, ApJ, 867, 151
Enßlin, T. A. 2019, AnP, 531, 1800127
Enßlin, T. A., & Frommert, M. 2011, PhRvD, 83, 105014
Enßlin, T. A., Frommert, M., & Kitaura, F. S. 2009, PhRvD, 80, 105005
Fiege, J. D., & Pudritz, R. E. 2000, MNRAS, 311, 85
Field, G. B., Goldsmith, D. W., & Habing, H. J. 1969, ApJL, 155, L149
Fukui, Y., Kawamura, A., Wong, T., et al. 2009, ApJ, 705, 144
Gaia Collaboration, Brown, A. G. A., Vallenari, A., et al. 2018, A&A, 616, A1
Galli, P. A. B., Bouy, H., Olivares, J., et al. 2020a, A&A, 634, A98
Galli, P. A. B., Bouy, H., Olivares, J., et al. 2020b, A&A, 643, A148
Galli, P. A. B., Loinard, L., Bouy, H., et al. 2019, A&A, 630, A137
Galli, P. A. B., Loinard, L., Ortiz-Léon, G. N., et al. 2018, ApJ, 859, 33
Goodman, A. A., Pineda, J. E., & Schnee, S. L. 2009, ApJ, 692, 91
Green, G. M., Schlafly, E., Zucker, C., Speagle, J. S., & Finkbeiner, D. 2019, ApJ, 887, 93
Green, G. M., Schlafly, E. F., Finkbeiner, D. P., et al. 2015, ApJ, 810, 25
Grenier, I. A., Casandjian, J.-M., & Terrier, R. 2005, Sci, 307, 1292
Grenier, I. A., Lebrun, F., Arnaud, M., Dame, T. M., & Thaddeus, P. 1989, ApJ, 347, 231
Großschedl, J. E., Alves, J., Meingast, S., et al. 2018, A&A, 619, A106
Haehn, D., Rannou, N., Ahtam, B., Grant, E., & Pienaar, R. 2014, in 5th INCF Congress of Neuroinformatics, ed. P. Holm (Stockholm: INCF), 8
Hall, K. P., Stanimirović, S., Lee, M.-Y., Wolfire, M., & Goldsmith, P. 2020, ApJ, 899, 23
Harris, C. R., Millman, K. J., van der Walt, S. J., et al. 2020, Natur, 585, 357
Heiles, C., & Troland, T. H. 2003, ApJ, 586, 1067

Hogg, D. W., Bovy, J., & Lang, D. 2010, Data Analysis Recipes: Fitting a Model to Data, arXiv:1008.4686
Hottier, C., Babusiaux, C., & Arenou, F. 2020, A&A, 641, A79
Jeffreys, H. 1939, The Theory of Probability (Oxford: Oxford Univ. Press)
Jordi, C., Gebran, M., Carrasco, J. M., et al. 2010, A&A, 523, A48
Knollmüller, J., & Enßlin, T. A. 2019, arXiv:1901.11033
Koch, E. W., & Rosolowsky, E. W. 2015, MNRAS, 452, 3435
Kounkel, M., Covey, K., Suárez, G., et al. 2018, AJ, 156, 84
Krumholz, M. R., McKee, C. F., & Tumlinson, J. 2008, ApJ, 689, 865
Krumholz, M. R., McKee, C. F., & Tumlinson, J. 2009, ApJ, 693, 216
Lada, C. J., Lombardi, M., & Alves, J. F. 2009, ApJ, 703, 52
Lada, C. J., Lombardi, M., & Alves, J. F. 2010, ApJ, 724, 687
Lallement, R., Babusiaux, C., Vergely, J. L., et al. 2019, A&A, 625, A135
Lee, M.-Y., Stanimirović, S., Murray, C. E., Heiles, C., & Miller, J. 2015, ApJ, 809, 56
Leike, R. H., & Enßlin, T. A. 2019, A&A, 631, A32
Leike, R. H., Glatzle, M., & Enßlin, T. A. 2020a, A&A, 639, A138
Leike, R. H., Glatzle, M., & Enßlin, T. A. 2020b, Galactic extinction within 400pc in cartesian coordinates v1.1, Zenodo, doi:10.5281/zenodo.3993082
Lombardi, M. 2009, A&A, 493, 735
Lombardi, M., & Alves, J. 2001, A&A, 377, 1023
Lombardi, M., Alves, J., & Lada, C. J. 2011, A&A, 535, A16
Marshall, D. J., Robin, A. C., Reylé, C., Schultheis, M., & Picaud, S. 2006, A&A, 453, 635
Moriarty-Schieven, G. H., & Wannier, P. G. 1997, ApJ, 475, 642
Muench, A. A., Lada, C. J., Luhman, K. L., Muzerolle, J., & Young, E. 2007, AJ, 134, 411
Murray, C. E., Peek, J. E. G., Lee, M.-Y., & Stanimirović, S. 2018a, ApJ, 862, 131
Murray, C. E., Stanimirović, S., Goss, W. M., et al. 2018b, ApJS, 238, 14
Nunez-Iglesias, J., Blanch, A., Looker, O., Dixon, M., & Tilley, L. 2018, PeerJ, 6, 4312
Ortiz-León, G. N., Loinard, L., Dzib, S. A., et al. 2018, ApJ, 865, 73
Ortiz-León, G. N., Loinard, L., Kounkel, M. A., et al. 2017, ApJ, 834, 141
Ostriker, J. 1964, ApJ, 140, 1056
Palmeirim, P., André, P., Kirk, J., et al. 2013, A&A, 550, A38
Panopoulou, G. V., Psaradaki, I., Skalidis, R., Tassis, K., & Andrews, J. J. 2017, MNRAS, 466, 2529
Pascucci, I., Edwards, S., Heyer, M., et al. 2015, ApJ, 814, 14
Planck Collaboration, Abergel, A., Ade, P. A. R., et al. 2011, A&A, 536, A25
Planck Collaboration, Aghanim, N., Ashdown, M., et al. 2016, A&A, 596, A109
Plummer, H. C. 1911, MNRAS, 71, 460
Rasmussen, C. E., & Williams, C. K. I. 2006, Gaussian Processes for Machine Learning (Berlin: Springer)
Rezaei Kh., S., Bailer-Jones, C. A. L., Hanson, R. J., & Fouesneau, M. 2017, A&A, 598, A125
Rezaei Kh., S., Bailer-Jones, C. A. L., Hogg, D. W., & Schultheis, M. 2018, A&A, 618, A168
Rezaei Kh., S., Bailer-Jones, C. A. L., Soler, J. D., & Zari, E. 2020, A&A, 643, A151
Rice, T. S., Goodman, A. A., Bergin, E. A., Beaumont, C., & Dame, T. M. 2016, ApJ, 822, 52
Robitaille, T., Beaumont, C., Qian, P., Borkin, M., & Goodman, A. 2017, Glueviz: Multidimensional Data Exploration v0.13.1, Zenodo, doi:10.5281/zenodo.1237692
Rosolowsky, E. W., Pineda, J. E., Kauffmann, J., & Goodman, A. A. 2008, ApJ, 679, 1338
Roy, N., Kanekar, N., & Chengalur, J. N. 2013, MNRAS, 436, 2366
Sale, S. E., Drew, J. E., Barentsen, G., et al. 2014, MNRAS, 443, 2907
Schlegel, D. J., Finkbeiner, D. P., & Davis, M. 1998, ApJ, 500, 525
Seifried, D., Haid, S., Walch, S., Borchert, E. M. A., & Bisbas, T. G. 2019, MNRAS, 492, 1465
Seifried, D., Walch, S., Girichidis, P., et al. 2017, MNRAS, 472, 4797
Skrutskie, M. F., Cutri, R. M., Stiening, R., et al. 2006, AJ, 131, 1163
Smith, R. J., Glover, S. C. O., & Klessen, R. S. 2014, MNRAS, 445, 2900
Smith, R. J., Treß, R. G., Sormani, M. C., et al. 2020, MNRAS, 492, 1594
Soler, J. D. 2019, A&A, 629, A96
Speagle, J. S. 2020, MNRAS, 493, 3132
Stanimirovic, S., Murray, C. E., Lee, M.-Y., Heiles, C., & Miller, J. 2014, ApJ, 793, 132
Sternberg, A., Le Petit, F., Roueff, E., & Le Bourlot, J. 2014, ApJ, 790, 10
Sullivan, C., & Kaszynski, A. 2019, JOSS, 4, 1450
Tang, N., Li, D., Heiles, C., et al. 2016, A&A, 593, A42
Tritsis, A., & Tassis, K. 2018, Sci, 360, 635
Turk, M. J., Smith, B. D., Oishi, J. S., et al. 2011, ApJS, 192, 9

Van der Swaelmen, M., Hill, V., Primas, F., & Cole, A. A. 2013, A&A, 560, A44

van der Walt, S., Schönberger, J. L., Nunez-Iglesias, J., et al. 2014, PeerJ, 2, e453

Virtanen, P., Gommers, R., Oliphant, T. E., et al. 2020, NatMe, 17, 261

Williams, J. P., Blitz, L., & Stark, A. A. 1995, ApJ, 451, 252

Williams, J. P., & Maddalena, R. J. 1996, ApJ, 464, 247

Wolfire, M. G., McKee, C. F., Hollenbach, D., & Tielens, A. G. G. M. 2003, ApJ, 587, 278

Yan, Q.-Z., Zhang, B., Xu, Y., et al. 2019, A&A, 624, A6

Zari, E., Lombardi, M., Alves, J., Lada, C. J., & Bouy, H. 2016, A&A, 587, A106

Zucker, C., Battersby, C., & Goodman, A. 2018a, ApJ, 864, 153

Zucker, C., & Chen, H. H.-H. 2018a, ApJ, 864, 152

Zucker, C., & Chen, H. 2018b, catherinezucker/radfil: RadFil: a Python Package for Building and Fitting Radial Profiles for Interstellar Filaments v1.1.1, Zenodo, doi:10.5281/zenodo.1481546

Zucker, C., Schlafly, E. F., Speagle, J. S., et al. 2018b, ApJ, 869, 83

Zucker, C., Speagle, J. S., Schlafly, E. F., et al. 2019, ApJ, 879, 125

Zucker, C., Speagle, J. S., Schlafly, E. F., et al. 2020, A&A, 633, A51